Dysfunction of Cortical GABAergic Neurons Leads to Sensory Hyper-reactivity in a *Shank3* Mouse Model of ASD

Qian Chen[1,†], **Christopher A. Deister**[2,†], **Xian Gao**[1,3], **Baolin Guo**[3,4], **Taylor Lynn-Jones**[1], **Naiyan Chen**[1], **Michael F. Wells**[3], **Runpeng Liu**[1], **Michael J. Goard**[5,6], **Jordane Dimidschstein**[3,7], **Shijing Feng**[8], **Yiwu Shi**[9], **Weiping Liao**[9], **Zhonghua Lu**[8], **Gord Fishell**[3,7], **Christopher I. Moore**[2,*], **Guoping Feng**[1,3,*]

[1]McGovern Institute for Brain Research, Department of Brain and Cognitive Sciences, Massachusetts Institute of Technology, Cambridge, MA, USA

[2]Department of Neuroscience, Brown University, Providence, RI, USA

[3]Stanley Center for Psychiatric Research, Broad Institute of MIT and Harvard, Cambridge, MA, USA

[4]Department of Neurobiology, School of Basic Medicine, Fourth Military Medical University, Xi'an, China.

[5]Department of Molecular, Cellular, and Developmental Biology, University of California, Santa Barbara, Santa Barbara, CA ,USA

[6]Department of Psychological & Brain Sciences, University of California, Santa Barbara, Santa Barbara, CA ,USA

[7]NYU Neuroscience Institute, New York University Langone Medical Center, New York, NY, USA

[8]Guangdong Provincial Key Laboratory of Brain Connectome and Behavior, The Brain Cognition and Brain Disease Institute, Shenzhen Institutes of Advanced Technology, Chinese Academy of Sciences, Shenzhen, China

*Corresponding author: Guoping Feng (fengg@mit.edu) and Christopher I. Moore (Christopher_moore@brown.edu) .
†These authors contribute equally to this work: Qian Chen and Christopher A. Deister

[9]Institute of Neuroscience and Department of Neurology of the Second Affiliated Hospital of Guangzhou Medical University, Key Laboratory of Neurogenetics and Channelopathies of Guangdong Province and the Ministry of Education of China, Guangzhou, 510260, China

Abstract

Hyper-reactivity to sensory input is a common and debilitating symptom in individuals with autism spectrum disorders (ASD), but the neural basis underlying sensory abnormality is not completely understood. Here we examined the neural representations of sensory perception in the neocortex of a *Shank3B*^{−/−} mouse model of ASD. Male and female *Shank3B*^{−/−} mice were more sensitive to relatively weak tactile stimulation in a vibrissa motion detection task. *In vivo* population calcium imaging in vibrissa primary somatosensory cortex (vS1) revealed increased spontaneous and stimulus-evoked firing in pyramidal neurons but reduced activity in interneurons. Preferential deletion of *Shank3* in vS1 inhibitory interneurons led to pyramidal neuron hyperactivity and increased stimulus sensitivity in the vibrissa motion detection task. These findings provide evidence that cortical GABAergic interneuron dysfunction plays a key role in sensory hyper-reactivity in a *Shank3* mouse model of ASD and identify a potential cellular target for exploring therapeutic interventions.

Introduction

Autism spectrum disorders (ASD) are highly heritable neurodevelopmental disorders, characterized by abnormalities in social interaction, repetitive behaviors, language and deficits in communication[1,2]. Atypical sensory responses are now part of the ASD diagnostic criteria (DSM-5). These sensory abnormalities are broad but include hyper-reactivity/ sensitivity to sensory input. Human fMRI[3] and animal model studies[4,5] suggest that cortical circuit abnormalities could contribute to altered sensory representations, but a direct demonstration of this has been lacking. Among the cell types implicated, cortical GABAergic interneurons are gaining more attention. Interneuron dysfunction has been observed in many animal models of ASD[4–7]. Further, recent work has linked GABAergic neuronal defects to multisensory integration deficits in mouse models of ASD[4,8]. However, a direct causal link between cortical GABAergic interneuron dysfunction and sensory abnormalities in ASD has not been established.

In this study, we used *Shank3B* knockout (*Shank3B*^{−/−}) mice[9] as a model to explore the neural mechanisms underlying sensory abnormalities. SH3 and multiple ankyrin repeat domains 3 (SHANK3) is a critical postsynaptic scaffolding protein that is required for glutamatergic synaptic development and function[10]. Deletions and mutations of the *Shank3* gene cause Phelan-McDermid syndrome with high prevalence of ASD. Genetic deletions/ mutations of the *Shank3* gene in mice leads to glutamatergic synaptic dysfunction and ASD-relevant behavioral abnormalities[9,11–14]. In this study, we trained *Shank3B*^{−/−} mice and their wild type (WT) littermates to perform a vibrissa motion detection task and found that *Shank3B*^{−/−} mice were more sensitive to weak vibrissa deflections. To test whether the hypersensitivity has a neocortical basis, we used *in vivo* two-photon calcium imaging to monitor neuronal activity in the somatosensory cortex of both WT and *Shank3B*^{−/−} mice. Calcium imaging revealed increased spontaneous and stimulus-evoked activity in pyramidal

neurons, but reduced activity in interneurons in *Shank3B*$^{-/-}$ mice. Preferential-deletion of *Shank3* from interneurons was also associated with pyramidal neuron hyperexcitability and sensory hypersensitivity. These data suggest that neocortical interneuron dysfunction in *Shank3B*$^{-/-}$ mice is key to the emergence of abnormal pyramidal neuron hyperexcitability and sensory hypersensitivity in this monogenic model of ASD.

Stimulus hyper-reactivity in *Shank3B*$^{-/-}$ mice

To investigate whether *Shank3B*$^{-/-}$ mice exhibit any deficits in tactile sensitivity we trained both *Shank3B*$^{-/-}$ mice and their WT littermates to perform a tactile detection task. Head-fixed and water restricted mice were presented with randomly timed periodic vibrissae deflections (Fig. 1a) and could earn a water reward by licking within a 'report window' that was timed to the onset of a stimulus (Fig. 1b, i). The frequency of the stimulus was fixed, but the strength was varied by scaling the amplitude (Fig. 1a, inset). The task was on a "go/no-go" format and thus had four possible trial outcomes: a 'hit' if the animal licked correctly in response to a stimulus, a 'miss' if the animal did not lick when a stimulus was presented, a 'false positive' if the animal licked in response to a zero-amplitude stimulus (catch-trial) or a 'correct rejection' if the animal correctly ignored a zero amplitude stimulus (Fig. 1b, ii). The ratio of hits to all stimulus trials, and the ratio of false positives to all catch-trials were used to determine the hit rate and false positive rates (or false alarm rates). Using these estimates of hit- and false-positive rates, the sensitivity index d-prime (*d'*) was determined for each animal. *d'* is a standard metric for scoring detection-sensitivity from signal detection theory[15–17], it is a metric that quantifies how separated an animal's responses to noise are from their responses to a true signal (Supplementary Figure1a). In addition to calculating *d'*, we determined the related metric 'criterion location' to quantify an animal's bias towards reporting true positives versus false positives (Supplementary Figure 1b). Criterion location is an important metric because animals can, in theory, improve their performance without a true change in sensitivity if they report more false positives (i.e., by guessing more often). We found no differences in the relationship between *d'* and criterion between WT and *Shank3B*$^{-/-}$ animals (Supplementary Figure 1c). Throughout the experiments, all littermate pairs of WTs and *Shank3B*$^{-/-}$ animals showed no differences in weight (mean weights ± s.e.m. of WT /*Shank3B*$^{-/-}$: first three sessions: 22.0 ± 3.0 grams/23.6 ± 3.7 grams; last three sessions: 21.6 ± 2.9/23.0 ± 3.9 grams; *p*=0.68 and *p*=0.54, n=10 in each group; bootstrap mean-difference test). Moreover, WT and *Shank3B*$^{-/-}$ mice did not show differences in their lick rates (Fig. 1d), which we assessed to rule out the potential of motor differences between WT and *Shank3B*$^{-/-}$ mice. Fig.1c shows lick rasters from a WT (Fig. 1c, top) and a littermate *Shank3B*$^{-/-}$ mouse (Fig.1c, bottom). The data shown in Fig.1c, which included all trials that showed no pre-stimulus licking, were compared across sessions and animals and showed no rate differences between WT and *Shank3B*$^{-/-}$ groups (Fig. 1d, i, left). We also found no difference in lick rates between WT and *Shank3B*$^{-/-}$ mice, even if trials with pre-stimulus licking were included (Fig. 1d, i, right). There was no significant difference in the total number of trials performed per session (Fig. 1d, ii, left). Moreover, there was no difference in the number of trials discarded due to pre-stimulus licking (Fig. 1d, ii, right), suggesting that both groups of mice had similar levels of impulsivity.

In order to compute d' and construct psychometric detection curves we first computed the hit-rate and false alarm rate for all stimuli across six sessions in which the animals experience with the task overlapped (Supplementary Figure 2a). Previous work has shown that somatosensory cortex contributes most to the detection of weak stimuli, closer to perceptual threshold[16,18]. Thus, we examined detection performance with respect to strong, readily detectable maximal stimuli (1 mm), and more ambiguous weak stimuli (0.2–0.5 mm) (Supplementary Figure 2). False alarm rates appeared similar for WT and *Shank3B*^{−/−} mice. We further analyzed the trials that comprised the last three overlapping sessions where performance had stabilized for all mice (Supplementary Figure 2). First, we examined sensitivity differences by computing d' for strong and weak stimuli. Maximal d' for *Shank3B*^{−/−} and WT animals was not significantly different (Fig. 1e, left). However, d' for weaker stimuli computed for the same behavioral sessions was significantly higher in *Shank3B*^{−/−} when compared to WT animals (Fig. 1e, right). We then constructed psychometric curves for *Shank3B*^{−/−} and WT mice (Fig. 1f) by determining hit-rates for a range of stimulus amplitudes. The psychometric curve of *Shank3B*^{−/−} mice show a leftward shift relative to WT mice. We quantified this shift by comparing the thresholds in our samples. We found that threshold for WT mice was significantly higher than that of *Shank3B*^{−/−} mice (Fig. 1f insets). Taken together, these data show that *Shank3B*^{−/−} mice are more sensitive to vibrissae stimuli than their WT counterparts are.

Increased spontaneous and stimulus-evoked neuronal activity in *Shank3B* [−/−] mice

To study network mechanisms underlying stimulus hypersensitivity in *Shank3B*^{−/−} mice, we performed large-scale *in vivo* two-photon calcium imaging in head-fixed awake WT and *Shank3B*^{−/−} mice. We used the excitatory-specific human CaMKIIα promotor to drive the expression of the genetically encoded calcium indicator GCaMP6f (referred throughout as GCaMP6)[19]. Our imaging fields contained 68–112 neurons (mean ± s.e.m.: 84±12). First, we compared the spontaneous GCaMP6 activity of vS1 between *Shank3B*^{−/−} and WT mice. Interestingly, we found that *Shank3B*^{−/−} mice showed higher calcium event rates compared to their WT counterparts (Fig. 2a & 2b). Between our sample groups, we observed a small, but significant, increase in pairwise correlation of spontaneous firing in *Shank3B*^{−/−} mice (Fig 2a, example traces; Fig 2c). It is well established that when neuronal rate increases correlations will increase as well, even beyond increases in chance spike overlap due to more spikes being discharged[18]. Although, many factors could lead to different correlations between neurons despite those neurons firing at the same rate under different conditions, one factor that has been previously studied is changing the balance of excitation and inhibition[20]. We studied the relationship between pairwise rate and correlations by computing the geometric pairwise mean and correlation for all pairs in each imaging session, we then pooled these data and took the mean and standard error of the mean for three overlapping rate bins (Supplementary Figure 3a). For WT mice there was a linear dependence on rate and correlation (linear fit; regression slope=0.2; p=0.03, linear regression F-Test). For *Shank3B*^{−/−}, the correlation/rate relationship was relatively flat across the rates examined (linear fit; regression slope=0.02, p=0.43, linear regression F-Test). These results suggest

that the correlation increases in *Shank3B*$^{-/-}$ are the result of circuit alterations and not just a simple rate change.

We next determined if stimulus-evoked responses were also enhanced in *Shank3B*$^{-/-}$ mice. We performed *in vivo* two-photon imaging of excitatory neurons as mice received randomly timed and variable amplitude piezo-driven vibrissa deflections (Fig. 2f, inset), just as in our detection task. Fig. 2d shows representative example that are the evoked-response from all stimulus-responsive neurons in a WT and *Shank3B*$^{-/-}$ imaging session. The average-proportion of stimulus responsive neurons found in WT mice was 0.26 ± 0.08 (mean ± s.e.m.), which is within the range of previous studies in awake vS1[21–23] However, the proportion of stimulus responsive neurons in *Shank3B*$^{-/-}$ mice was significantly higher at 0.52 ± 0.11 (Fig. 2e, mean ± s.e.m.).In addition to an increase in the proportion of stimulus responsive neurons in *Shank3B*$^{-/-}$ mice compared to WT, we found enhanced evoked responses across most of the range of stimulus-amplitudes used in our detection task. To quantify this, we constructed an average peri-stimulus time histograms (PSTHs, see the methods) for WT and *Shank3B*$^{-/-}$ mice (Fig. 2f). Visual comparisons of the WT and *Shank3B*$^{-/-}$ PSTHs showed clear differences, with an overall enhancement of *Shank3B*$^{-/-}$ activity. In order to more quantitatively compare these differences, we plotted the mean peak evoked-response (Fig. 2g) for both WT and *Shank3B*$^{-/-}$. The strongest and weakest deflections showed no significant difference (Fig. 2g). As in our behavior, we found the largest differences in evoked responses around the intermediate stimulus range. These results show that layers II/III pyramidal neurons in vS1 of *Shank3B*$^{-/-}$ are more active and sensitive to external stimuli.

Shank3B$^{-/-}$ mice showed hypo-neuronal activity in inhibitory somatosensory cortical neurons

Shank3 is a major scaffolding protein at glutamatergic synapses, coordinating the recruitment of many postsynaptic signaling molecules[10,24]. Our group and others have shown that *Shank3* deletion causes a reduction in glutamatergic synaptic transmission[9,11,14,25]. We were intrigued by our calcium imaging results that showed increased activity of cortical pyramidal neurons in *Shank3B*$^{-/-}$ animals. Sparse stimulus evoked activity in layers II/III of WT vS1 is known to be dependent upon stimulus-evoked feedforward inhibition[22,26,27], which is a mechanism that 'balances' stimulus-evoked feedforward excitation using strong, time-lagged inhibition[26–28]. Recently, deficits in parvalbumin circuits within the insular cortex and vS1 of *Shank3B*$^{-/-}$ mice have been reported[4,29]. We hypothesized that inhibitory circuit disruption in somatosensory cortex may cause excitatory neuron hyperactivity in *Shank3B*$^{-/-}$ mice. To test this, we performed two-photon calcium imaging selectively from inhibitory neurons of the vS1. We performed unilateral injections of AAVs expressing GCaMP6 under the control of the GABAergic interneuron-specific Dlx5/6 promoter, a recently developed tool for GABAergic interneuron-specific expression[30]. We injected AAV-Dlx5/6-GCaMP6 into vS1, which resulted in selective expression of GCaMP6 in inhibitory neurons of vS1. As predicted, Shank3B$^{-/-}$ mice showed reduced spontaneous calcium event rates (Fig. 3a & 3b). Correlations in the spontaneous firing of inhibitory neurons in WT and *Shank3B*$^{-/-}$ mice were more

pronounced than excitatory neurons (Fig 3a, example traces; Fig 3c). Because we observed a significant decrease in firing rate of inhibitory neurons, an increase in correlations is not likely the result of a simple change in the rate of the population. We studied the relationship between rate and correlation and found this relationship was not simply linear in either WT or *Shank3B*$^{-/-}$ mice (Supplementary Figure 3b). It shows high correlations between low-rate pairs and high-rate pairs, whereas moderate-rate pairs have low correlations. Overall, there was an increase in mean correlation among low and high rate pairs in *Shank3B*$^{-/-}$ mice.

We also examined stimulus-evoked activity in inhibitory cells, as we had for excitatory cells (Fig. 3d). We found the number of stimulus responsive neurons was significantly reduced in *Shank3B*$^{-/-}$ mice (Fig. 3e). Further, a comparison of PSTHs constructed from all stimulus-responsive inhibitory cells in WT and *Shank3B*$^{-/-}$ neurons revealed that over most of the stimulus-range *Shank3B*$^{-/-}$ inhibitory cells showed significantly lower-magnitude responses than WT mice (Fig.3f, and 3g). Thus, inhibitory neurons in vS1 of *Shank3B*$^{-/-}$ are hypoactive.

Preferential *Shank3* deletion in vS1 inhibitory neurons also causes inhibitory neuron hypo-excitability and excitatory neuron hyper-excitability

It remains unclear whether *Shank3* deletion in interneurons is the cause of the hyperactivity of the pyramidal neurons, or the downregulation of interneuron activity is an indirect byproduct of a lifetime of abnormal circuit development in these mice. To address this, we aimed to delete *Shank3* in the inhibitory neurons of vS1 using the Dlx5/6 promotor-driven Cre recombinase in the *Shank3B* conditional mice (*Shank3B*$^{fl/fl}$) which we generated[29]. Previously, the Dlx5/6 promotor was characterized to be highly selective in expressing fluorescent and optogenetic-proteins in inhibitory neurons, but its ability to restrict Cre-expression to inhibitory cells was not found to be consistent in all cases, because trace amount of Cre could be sufficient for recombination[30]. To determine how selective an AAV-Dlx5/6-Cre-mKate2 (Dlx5/6-Cre) construct is at deleting *Shank3* in interneurons, we performed single-cell PCR from neighboring inhibitory and excitatory layer II/III vS1 neurons (Supplementary Figure 4). We screened 42 excitatory neurons and 33 inhibitory neurons from three AAV-Dlx5/6-Cre injected *Shank3B*$^{fl/fl}$ mice. *Shank3* was deleted in every inhibitory neuron examined. However, $23.15\pm3.34\%$ of the excitatory neurons also showed *Shank3* deletion. Thus, the use of the Dlx5/6-Cre construct in vS1 of *Shank3B*$^{fl/fl}$ mice leads to preferential deletion of *Shank3* in inhibitory interneurons.

For controls, we used a construct in which the catalytic domain of Cre recombinase was deleted (AAV-Dlx5/6- Cre-mKate2, Dlx5/6- Cre). We used AAV-Dlx5/6-GCaMP6 to monitor activity of inhibitory neurons in vS1. Strong GCaMP6 signal in layer II-III inhibitory neurons was detected by two-photon microscopy in both Dlx5/6- Cre and Dlx5/6-Cre virus injected *Shank3B*$^{fl/fl}$ mice (Fig. 4a). Compared with Dlx5/6- Cre-injected *Shank3B*$^{fl/fl}$ mice, those neurons infected with Dlx5/6-Cre showed significantly lower calcium event frequency among inhibitory neurons, similar to that seen in *Shank3B*$^{-/-}$ mice (Fig.4a & 4b).We observed an increase in spontaneous activity correlations among inhibitory cells (Fig.4a, example traces; Fig.4c), just as we did for inhibitory cells in the *Shank3B*$^{-/-}$

mouse. The relationship between rate and correlation for inhibitory neurons in the local knockout condition was very similar to that of the *Shank3B*$^{-/-}$ mouse, but overall the differences between Dlx5/6- Cre and Dlx5/6-Cre injected mice were more pronounced (Supplementary Figure 3c). Also similar to *Shank3B*$^{-/-}$ mice, Dlx5/6-Cre injected (local *Shank3B* knockout) mice showed more lower-rate pairs with higher correlations, and some high-rate pairs that also showed increases.

We also examined stimulus-evoked activity in inhibitory neurons in those mice. The proportion of stimulus responsive neurons was significantly reduced in Dlx5/6-Cre-injected *Shank3B*$^{fl/fl}$ mice (Fig 4d & 4e). PSTHs show reduced evoked activity in Dlx5/6-Cre-injected, relative to Dlx5/6- Cre-injected *Shank3B*$^{fl/fl}$ mice (Fig. 4f). These differences were significant for all of the stimulus amplitudes (Fig. 4g). These results show that preferential deletion of *Shank3* in GABAergic interneurons can cause hypoactivity of in layer II-III interneurons of vS1.

After establishing that *Shank3* deletion from inhibitory cells causes the hypo-excitability of interneurons, we hypothesized that the excitability of excitatory neurons would be increased consequently. To test this, we used the same Dlx5/6-Cre and Dlx5/6- Cre strategy to delete *Shank3* from vS1 inhibitory neurons, but also monitored GCaMP6 activity in excitatory neurons by driving its expression via the CaMKII promoter (Fig. 5a). As we predicted, the frequency of spontaneous Ca^{2+}−events was dramatically increased in Dlx5/6-Cre-injected *Shank3B*$^{fl/fl}$ mice (Fig. 5b&5c and Supplementary Videos 1 & 2). In addition to an increase in excitatory neuron firing rates in the local knockout condition, we found that correlations in spontaneous firing was significantly increased in Dlx5/6-Cre-injected compared to Dlx5/6- Cre-injected *Shank3B*$^{fl/fl}$ mice. (Fig 5b, example traces; Fig 5d). For Dlx5/6- Cre - injected *Shank3B*$^{fl/fl}$ mice there was a linear dependence on rate and correlation (Supplementary Figure 3d; linear fit; regression slope=0.21 *p*=0.03, linear regression F-Test). For Dlx5/6-Cre -injected *Shank3B*$^{fl/fl}$ mice, the correlation/rate relationship was relatively flat across the rates examined (linear fit, regression slope=0.02, *p*=0.6, linear regression F-Test). These results are similar to those observed in WT/*Shank3B*$^{-/-}$ comparison, but the increase in correlations are higher in the local *Shank3B* knockout.

Evoked activity was also increased in excitatory neurons of Dlx5/6-Cre-injected mice. The proportion of excitatory neurons that were stimulus responsive was significantly higher in Dlx5/6-Cre-injected mice (Fig. 5e & Fig 5f). Further, comparisons of stimulus-responsive neuron's PSTHs showed significant increases in the magnitude of vibirssa-evoked activity across all the stimulus amplitudes examined (Fig. 5g and 5h). Taken together, these results support the hypothesis that deletion of *Shank3* in interneurons results in a reduction of cortical inhibition and thereby increasing the amount of excitation in the cortical circuit.

Preferential deletion of *Shank3* in interneurons causes stimulus hyper-reactivity

It remains unclear if vS1-specific hyperexcitability will also lead to sensory hypersensitivity. To directly test this we trained *Shank3B*$^{fl/fl}$ animals injected with AAV-Dlx5/6-Cre-mKate2 and injected with AAV-Dlx5/6- Cre-mKate2 for the detection task. The injected animals

showed similar unilateral spread of Cre or ΔCre as measured by post-hoc examination of mKate2 expression in fixed tissue (Fig. 6a and Supplementary Figure 5).

Similar to the results from WT and *Shank3B*$^{-/-}$ mice, we found that the relationship between apparent sensitivity (*d'*) and response bias were the same between Dlx5/6-ΔCre and Dlx5/6-Cre-injected mice (Supplementary Figure 6). We also found no difference in weights between groups throughout the experiments (mean weights ± s.e.m. of Dlx5/6-Cre and Dlx5/6-ΔCre: First three sessions: 24.7 ± 2.6 grams; 23.3 ± 3.2 grams, n= 6 mice in each group; *p*=0.8, bootstrap mean-difference test; Last three sessions: 23.9 ± 2.4; 23.0 ± 3.1 grams, n= 6 mice in each group; *p*=0.8, bootstrap mean-difference test). Lick rates determined on just the analyzed trials which did not include those with pre-stimulus licks, or when we computed lick rate including discarded trials with pre-stimulus licks were not significantly different between Dlx5/6-ΔCre and Dlx5/6-Cre-injected mice (Fig. 6b, i). The average number of trials per session included for analysis were not different (Fig. 6b, ii, *left*), nor were the number of trials discarded per session (Fig. 6b, ii, *right*). To determine if Dlx5/6-Cre-injected mice were more sensitive than Dlx5/6-ΔCre, we computed *d'* for strong and weak stimuli. *d'* for strong and weak stimuli. Maximal *d'* for Dlx5/6-ΔCre and Dlx5/6-Cre was significantly different (Fig. 6c, *left*). Further, *d'* for weaker stimuli computed for the same behavioral sessions was also significantly different between Dlx5/6-ΔCre and Dlx5/6-Cre animals (Fig. 6c, *right*). The psychometric curve of the Dlx5/6-Cre-injected mice was leftward-shifted (Fig. 6d) indicating that their response rates to weaker stimuli are greater than Dlx5/6-ΔCre-injected mice. As predicted, Dlx5/6-Cre-injected mice had a lower threshold than Dlx5/6-ΔCre-injected mice (Fig. 6d inset).

Because we observed leakage of Dlx5/6-driven Cre expression in ~20% excitatory neurons we set out to determine what effect sparse and selective deletion of *Shank3* from vS1 excitatory neurons, if any, would have on firing rates and detection behavior. We used diluted virus to titrate our injections and achieved ~40% infection of AAV-CaMKII-ΔCre-mKate2 (CaMKII-ΔCre) or AAV-CaMKII-Cre-mKate2 (CaMKII-Cre) excitatory neurons in vS1 of *Shank3B*$^{fl/fl}$ mice (Supplementary Figure 7a & 7b). We found that the spontaneous activity and evoked response of excitatory neurons in CaMKII-Cre injected *Shank3B*$^{fl/fl}$ mice were significantly reduced (Supplementary Figure 7c & 7d–g). Overall detection performance was also reduced in *Shank3B*$^{fl/fl}$ mice injected with CaMKII-Cre. The psychometric curve for CaMKII-Cre-injected *Shank3B*$^{fl/fl}$ mice (n=9 mice) showed an in-significant increase in threshold relative to CaMKII-ΔCre-injected *Shank3B*$^{fl/fl}$ mice (Supplementary Figure 7h). However, there was a reduction in performance of CaMKII-Cre injected *Shank3B*$^{fl/fl}$ mice (Supplementary Figure 7h). These data suggest that deletion of *Shank3B* just in a proportion of excitatory neurons does not improve stimulus sensitivity, as we observed in *Shank3B*$^{-/-}$ mice or the interneuron-biased local *Shank3B* knockout. Consistent with this, CaMKII-Cre and CaMKII-ΔCre-injected mice showed similar *d'* values for strong and weak stimuli (Supplementary Figure 7i). The reason we observed a rightward shift in the psychometric curve without a reduction in *d'* was because false-alarm rates and stimulus-response rates were lowered by a similar proportion. Thus, *Shank3B* deletion in excitatory neurons leads to reduced spontaneous and evoked activity in excitatory neurons, as well as blunted detection behavior. Both of these results are qualitatively opposite of those

observed in the *Shank3B*$^{-/-}$ mice, and the interneuron-biased local *Shank3B* deletion condition.

We next sought to determine if down regulation of inhibition alone was sufficient in explaining the results seen in network dynamics and detection performance observed in *Shank3B*$^{-/-}$ mice. To determine this, we used an inhibitory chemogenetic approach. We injected an AAV-Dlx5/6-hM4Di in vS1 of WT mice. We made acute in-vitro slices to determine the effectiveness of our Dlx5/6-hM4Di construct, and the DREADDs-agonist C21 (Supplementary Figs. 8a&b). We then imaged the activity of excitatory neurons using CaMKII-GCaMP6 *in vivo* from Dlx5/6-hM4Di-injected mice and trained them to perform the detection task. After mice showed proficiency in the task, we injected mice with the hM4Di agonist C21 (2 mg/kg) and imaged spontaneous and evoked neural activity as well as their performance on the detection task. We found an increase in spontaneous, evoked activity and correlation among excitatory neurons (Supplementary Figs. 8c–h), just as we had in the *Shank3B*$^{-/-}$ condition, and the local Dlx5/6-driven *Shank3B* deletion. Chemogenetically-driven inhibitory neuron downregulation led to markedly similar effects on detection-task performance as the local inhibitory-neuron biased *Shank3B* knockout condition. We found that the *d'* for strong and weak whisker deflections were increased after injecting the DREADDs-agonist C21 (Fig. 6e). Psychometric curves showed a significant leftward-shift after C21 injection (Fig. 6f). This result is consistent with precious findings in vS1 that optogenetically reducing the PV neuronal activity can enhance the mouse performance in detection task[31]. These results demonstrate that preferential deletion of *Shank3* from vS1 interneurons is sufficient to drive behavioral sensory hyper-reactivity.

Discussion

Sensory hypersensitivity has been observed in several mouse models of ASD and related neurodevelopmental disorders, including *Mecp2*$^{-/-}$ and *Fmr1*$^{-/-}$ [4,7] mice. Recent studies in ASD mouse models of *Mecp2*, *Shank3* and *Gabrb3* have shown that peripheral sensory neuron dysfunctions contribute to somatosensory defects including gentle touch[8,29]. Our results show that deficits in central nervous system circuits significantly contributes to sensory abnormalities in *Shank3B*$^{-/-}$ mice. The sensory hypersensitivity in *Shank3B*$^{-/-}$ mice correlates with a hyper-activity of cortical pyramidal neurons. Preferential deletion of *Shank3* in cortical inhibitory neurons is sufficient to cause a hyper-active cortical pyramidal neuron network and sensory hyper-reactivity. Impaired inhibitory neuron function has also been found in many other models of ASD[4,32,33]. Our current study provides evidence that dysfunctional excitatory synaptic transmission in cortical interneurons likely results in their hypo-activity and consequently contributes to sensory hyper-reactivity in the *Shank3* mouse model of ASD.

A significant proportion of autistic individuals experience perceptual abnormalities[2,34,35]. Although *Shank3* expresses throughout the brain, it is enriched at both cortico-striatal and cortico-cortical synapses[9,36,37] and could lead to deficits in both local and long-range cortico-cortical interactions. Recent work[4,38] indicated that the cortex of *Shank3B*$^{-/-}$ mice is in a hyperexcitable state throughout early development, ultimately contributing to abnormal associative interactions between cortex and striatum. In order to further understand the

mechanisms responsible for the hyper-excitable state of *Shank3B*^{−/−} mice, we focused on somatosensory cortex and used a head-fixed 'go/no-go' based sensory detection task to probe perceptual disruptions in *Shank3B*^{−/−} mice. These experiments showed an intrinsic stimulus sensitivity enhancement in *Shank3B*^{−/−} mice. We found that motivational variables such as lick rates and criterion were similar across WT and *Shank3B*^{−/−} animals and thereby allowed for fair comparisons of sensitivity measures across groups. The relatively short training time needed for WT animals to learn the detection task may prove to be an essential feature for probing perceptual abnormalities in disease models[15,17].

In addition to changes in rate among excitatory and inhibitory neurons, we observed increases in pairwise correlations between both types of cells in *Shank3B*^{−/−} mice. For the excitatory neurons, we found both a net increase in rate and correlations. It has been established in the theoretical literature that rate and correlation are inexorably linked, at least when neurons are driven to fire at different rates with excitation alone[18]. We found a significant relationship between rate and correlation among excitatory neurons in WT mice, but this relationship was altered to some degree in *Shank3B*^{−/−}, and the local Dlx5/6-Cre-driven *Shank3B* knockout mice. The specific cellular and network-level reasons for this correlation change, and its importance, remains to be determined. However, excitatory and inhibitory conductance could influence neuronal correlations differently[20]. Therefore, it is possible that the increased correlations among excitatory neurons we observed reflects a reduction in inhibition driven by *Shank3* deletion. We also observed a net increase in correlations among inhibitory neurons in the knockout conditions, and in those cases, the average rates were significantly decreased. Since inhibitory neurons are strongly coupled to each other, and inhibitory neuron activity is reduced when *Shank3* is deleted, we can hypothesize that the overall trend for correlations to increase among inhibitory cells is also due to a reduction of inhibitory conductance among them. Our data do not address why there is a group of low firing rate inhibitory neurons with very high correlations in the WT mouse in the first place, and if they are truly distinct from the higher firing rate inhibitory neurons. What possible benefit, or disruption, correlation and/or synchrony changes may have for autistic mouse models of cortical sensory processing, that are independent of rate alone, is an interesting topic, but our data only begins to approach.

The disruption of E-I balance has been implicated in schizophrenia, autism and intellectual disabilities. It has previously been suggested[39] that autism and other related disorders might reflect an increase in the ratio between excitation and inhibition that leads to hyperexcitability of cortical circuits. Similarly, E-I balance is thought to be disrupted in epilepsy. It is worth noting that autistic individuals develop epilepsy at a rate up to 25 times that of the general population[40]. We did not observe spontaneous epileptic seizures in *Shank3B*^{−/−} mice. Nevertheless, excitatory neurons of primary sensory cortex (S1) were hyper-excitable and interneuron activity was reduced, suggesting a disruption of E-I balance. Furthermore, we found in *Shank3B*^{−/−} mice showed differences in perceptual performance and evoked-responses of the excitatory neurons only for weaker whisker deflections, not in strong deflections. However, there was a difference in the evoked-response of inhibitory neurons in *Shank3B*^{−/−} mice even for strong stimuli. And also, we found difference in perceptual performance and evoked-responses of the excitatory neurons both in weaker and strong deflections where we knocked *Shank3B* from just vS1 interneurons of adult mice.

Together, these results suggest that the nervous system of $Shank3B^{-/-}$ mice may have compensated during development in order to normalize the representations of strong sensory stimuli despite having less inhibition to work with. There are many possible ways to achieve this, one parsimonious explanation is lemniscal-thalamic drive to S1 may have been downregulated in development to achieve similar sensory responses in cortex for the most unambiguous stimuli. Understanding more of how the central nervous system contributes as a whole to ASD-phenotypes is an interesting topic for further study.

Methods:

Animal Use

All experiments were conducted under the guidelines of the Division of Comparative Medicine, with the protocol approved by the Committee for Animal Care of the Massachusetts Institute of Technology. $Shank3B^{-/-}$ and $Shank3$ conditional knockout mouse line was generated by our lab as described in previous study[9,29] and bred in house on a 12 h light/dark cycle (lights on at 7:00, lights off at 19:00) with food and water available ad libitum. A mix of male and female C57BL/6 mice (4~6-month-old) were used for experiments. All experiments using $Shank3B^{-/-}$ mice were performed in age matched littermates from breeding pairs between $Shank3B^{+/-}$ heterozygous animals. All animal experiments and data analysis were performed with experimenters blinded to genotypes.

Un-cued tactile Behavioral test

Surgeries: On the day of surgery, mice were induced into an anesthetic state with 3% isoflurane (in O_2) and injected with 0.1 mg/kg IP buprenorphine (an opiate analgesic). Meloxicam (1 mg/kg, subcutaneous) was administered pre-operatively and every 24 hours for 3 days to reduce inflammation. Isoflurane was lowered until mice reached a stable anesthetic plane; at which time the isoflurane was typically 1.5–2 %. The head is shaved from the nasal septum up to the occipital bone (between ears) and ointment is applied to each eye. The mouse is positioned in a stereotactic head holder/gas mask. The surgical area is cleaned by 70 % alcohol and 2 % iodine solution. The scalp overlying the dorsal skull was removed. The periosteum was removed with a scalpel. An autoclaved titanium headpost was cemented to the exposed skull using strong dental cement (C&B Metabond; Parkell). After head plate implantation, mice recovered for at least five days before beginning water restriction. ~4–6-month-old male and female WT (n=15) and $Shank3B^{-/-}$ (n=17) mice used for behavior test. For locally deleting $Shank3B$ from the interneurons in vS1, ~4-month-old male and female $Shank3B^{fl/fl}$ mice (n=11) were unilaterally injected with $AAV_{2/8}$-Dlx5/6-Cre-mKate2 or $AAV_{2/8}$-Dlx5/6- Cre-mKate2 (control, n=11) in vS1and the head plate was implanted. For locally deleting $Shank3B$ from the excitatory neurons in vS1, ~4-month-old male and female $Shank3B^{fl/fl}$ mice were unilaterally injected with $AAV_{2/8}$-CaMKII-Cre-mKate2 (n=9) or $AAV_{2/8}$-CaMKII - Cre-mKate2 (control, n=7). For chemogenetic inhibition of inhibitory neurons in vS1, 3~4-month-old male and female wide type mice were unilaterally injected with $AAV_{2/9}$-Dlx5/6-hM4Di-p2a-nlsdTomato(n=8) or $AAV_{2/9}$-Dlx5/6-dTomato-p2a-nlsdTomato (control, n=8). Mice recovered for two weeks to let the virus expression before the beginning of water restriction.

Behavior/Water-Restriction: Animals were placed on water-restriction for at least seven days (1~1.25 ml/day) prior to training. We interacted with animals almost daily as they were habituated to the behavioral apparatus and the researcher. Whiskers were restrained by placing them in a hoop made from silk suture thread that was closed 2–3 mm from the base of the whiskers. This restrainer was attached to a piezo-electric plate bender (Noliac; CMBP09). At the beginning and end of each session, we confirmed that the restrainer was in the same place and held the same whiskers as when the experiment started. On the first two day of training, we focused on associating licking from an acrylic lick-port with whisker stimulation. After this conditioning session (100–200 trials), mice performed our behavioral task with 300–400 trials of mostly highly perceptible stimuli. Once they displayed proficiency with the task (signal detection statistic for strong stimuli, d'>1), all sessions were converted to 20 % catch trials and stimuli drawn from a random interval allowing for coverage over their entire perceptible range. Mice typically ran 12–14 sessions before being taken off water restriction. The data collection was randomized. Mice were rotated across behavioral rigs between each session to avoid any biasing of behavior toward a specific rig. Further, the training sequence of the animals was randomized across training days. For the chemogenetic manipulations, mice were trained 11 sessions before the administration of the C21[41] (2mg/kg, Intraperitoneal injection, HelloBio). From 12 to 14 sessions, mice were administrated with C21 one hour before the training.

Behavioral control was conducted using custom routines written in MATLAB (Mathworks) to interface with National Instruments DAQ boards. The piezo actuator was controlled by piezo driver (Noliac). The stimulus was a 20 Hz train of ten stimuli that each consisted of a fast cosine wave onset with a time to peak of 6 ms (from caudal to rostral) and a slow cosine return with a time to peak of 20 ms (from the deflected rostral point back to rest). For maximum-amplitude deflections, vibrissae moved approximately 1 mm at the point of contact. The stimulation amplitudes were calibrated using a high-speed camera. Lick detection was made using an IR emitter/receiver pair (SparkFun; SEN-00241) centered across the tip of the lick-spout; the IR pair was calibrated daily. Solenoid valves (NResearch Inc.; 161T011) gated water flow and vacuum return.

There were no stimulus cues and all behavior were done in a dark room with white masking noise present. Stimulus timing was essentially random: each trial had a fixed time of 8 seconds from a behavioral control perspective, but we randomly chose a time to insert a stimulus between 1 and 6 seconds after trial onset. The stimulus amplitude was chosen randomly except for catch-trials (stimulus amplitude = 0 mm) and maximal stimuli (stimulus amplitude = 1mm were interleaved randomly, but had a fixed frequency. In addition, any false alarms (licking during the report window on a catch trial) led to 20 second time out.

Data analysis: No mice or data points from our experimental groups were excluded from analysis. Trials were included for analysis from behavioral sessions in which mice just began to show proficiency in the task, were engaged with the task, and completed at least fifty trials without pre-stimulus licking. We excluded trials where animals licked 500 ms before the onset of a stimulus. Trials for detection tasks are not initiated by the subject. Thus, the number of trials that mice would complete in a session was dependent on their experience and motivation. We had a maximum amount of time would allow any mouse to stay on a rig,

but all mice would complete their trials before this time elapsed. However, because the number of trials each mouse would complete was variable, we allowed mice to run until they abstained from licking over a large block of trials, regardless of how detectable the stimulus was, which we interpreted as the animal disengaging from the task. In some cases, a mouse would disengage for a noticeable block of trials, but then re-engage. We developed an empirical method to detect the period(s) in which the mouse disengaged from the task and used it to set an "engagement threshold" to exclude disengaged trials. This method involved taking the moving average of the binary responses and stimulus amplitude using a 50-trial wide window. This resulted in a time-series showing 50-trial wide trends in response probability and stimulus amplitude fluctuations. As mice reached the end of a session, their average response rate would begin to slowly drift towards zero and skew the response distribution towards zero. We empirically determined that the amount of skew (difference in median and mean) of the stimulus distribution, relative to its bottom-third was similar to the proportion of skew in the response distribution and its bottom third when disengaged trials at the end of a session were manually removed. Thus, we defined an engagement threshold as the bottom third of the response distribution corrected for the proportional difference between its statistics and that of the stimulus distribution. Any block of trials that were below this line were excluded from analysis.

Psychometric curve construction: Psychometric curves show the relationship between stimulus amplitude and detection rate. To test if these curves were different between *Shank3B*$^{-/-}$ mice we compared the mid-points (threshold) and slope-factors (k) of the curve fits for each mouse. The "threshold" in this case corresponds to the deflection amplitude that leads to a successful report more than half of the time, relative to the false alarm rate. We binned responses (hits or misses) based into one of five stimulus amplitude bins. We similarly grouped false-alarms and correct rejections for all catch-trials (trials with a zero-amplitude stimulus). We computed the hit-rate for each amplitude bin, and the false-alarm rate and fit a sigmoidal function to the resulting amplitude vs. response rate data. The sigmoidal function of the form: $y = max/(max + e^{(threshold-X)/slopeFactor})$. Where X is the independent variable (stimulus amplitude) and the fit parameters are: a) the threshold which is the amplitude that leads to 50% of the maximal response, b) max, which is the maximal response, and c) slope-Factor, which is the slope of the resulting sigmoid near the threshold. Curve fits were performed in MATLAB using a Non-linear least squares method. All fits had an adjusted R-squared >0.95 and a threshold within our stimulus range.

Virus injection and cranial window preparation

Mice were anesthetized using isoflurane (3% for induction, 1.5–2% during surgery). and injected with 0.1mg/kg IP buprenorphine (an opiate analgesic). Meloxicam (1mg/kg, subcutaneous) was administered pre-operatively and every 24 h for 3 days to reduce inflammation. The head is shaved from the nasal septum up to the occipital bone (between ears) and ointment is applied to each eye. The mouse is positioned in a stereotactic head holder/gas mask. The surgical area is cleaned by 2 % iodine and 70 % alcohol solution. The scalp overlying the dorsal skull was removed. The periosteum was removed with a scalpel. A 3 × 3 mm piece of skull was removed above the somatosensory cortex as determined by stereotactic coordinates, and the dura was kept intact and moist with saline.

To express GCaMP6f in pyramidal neurons of the primary somatosensory cortex, adeno-associated virus $AAV_{2/8}$ carrying the construct CaMKII-GCaMP6f (GCaMP6f under the neural-specific human CaMKIIα promoter, 1×10^{12} genome copies/ml) was injected at a depth of ~200 μm to the primary somatosensory cortex (5~6 sites, the center of the injection area is : 1.5 mm post the lambda suture , 2.5 mm from the mild line suture) of adult male and female C57BL/6J WT and *Shank3B*$^{-/-}$ mice (4–6-month-old, n=6 in each groups). For expression of GCaMP6 in GABAergic neurons, GCaMP6 in AAV2/8 under the Dlx5/6 promoter adeno-associated virus was injected in the primary somatosensory cortex of 4–6-month-old male and female WT and *Shank3B*$^{-/-}$ mice (n= 6 in each groups). For conditional knockout *Shank3* in interneurons and imaging neuronal activity in inhibitory or excitatory neurons in *Shank3B*$^{fl/fl}$ mice, $AAV_{2/8}$-Dlx5/6-GCaMP6 or $AAV_{2/8}$-CaMKII-GCaMP6 virus and AAV-Dlx5/6-Cre-mKate2 were injected in to the somatosensory cortex at a ratio of 1: 3. Small volumes (~20 nl) of viral suspension were delivered over a period of 5 min per site using a Nanoject II micro-injector (Drummond scientific, Broomall, PA, USA).

For the cranial window, two coverslips were joined with ultraviolet curable optical glue (NOR-138, Norland). A smaller (3 mm diameter) insert fit into the craniotomy and a larger piece (5mm diameter) was attached to the bone. A custom-designed head plate was cemented on the cranial window with Meta-bond (Parkell).

In vivo two-photon calcium imaging

To reduce the anxiety behavior related to the head fixed strategy, we let the animal adapt the imaging environment prior to imaging. Two weeks after viral injection mice were moved to two-photon imaging room and each mouse was head fixed on a custom-made mouse strain system for 30 min, once per day for five days. For each imaging experiment, mice were head-fixed in the restraint and placed under the two-photon microscope for 15 min before the experiments started. Mice were imaged two rounds of spontaneous firing without whisker stimulation. And the mice were imaged with the whisker stimulation driven by piezo after the mice trained (4~5 weeks after virus injection). The stimulation method and rigs were identical to the tactile detection behavior test.

In vivo two-photon imaging was performed as described previously[42]. Briefly, the imaging was performed on a custom two-photon laser-scanning microscope (Ultima; Bruker) coupled with a Mai Tai Deep See laser (Spectra Physics). The laser was operated at 910 nm (~30–40 mW average power on the sample). The emission filter set for imaging GCaMP6 fluorescence consisted of a 575-nm dichroic mirror and a 525/70 nm band-pass filter. Fluorescence signal was detected using Hamamatsu multialkali PMTs. In most experiments, images were acquired at frame rates of 10 Hz at a resolution of 128×100 pixels using a 20×, 1.0 NA water-immersion objective (Zeiss). Image acquisition was performed using custom Prairie View Software. Fifteen minutes of spontaneous activity were collected to estimate the occurrence and duration of spontaneous events. Then, the same stimuli used in the un-cued tactile behavioral test were delivered to the contralateral whiskers and GCaMP6 signals were simultaneously recorded.

Calcium Imaging Data analysis

Images were analyzed *post-hoc* using a custom program, and open-source routines, written using MATLAB (MathWorks). The package has been used elsewhere[43], and available via GitHub (https://github.com/cdeister/imageAnalysis_gui). Frames were collected as individual image files. For analyses of spontaneous calcium events, we collected 8752 images per mouse at 10Hz. We analyzed the first ten minutes of each recording to compute event rate, which comprise 6000 images per mouse. For analyses of stimulus-evoked response, 70 images were acquired for 300 trials for a total of 21000 frames per mouse. Most motion artifacts came from small movements in the x-y plane. Because our acquisition rate was faster than the average frequency of mouse movements, we relied on rigid-body methods to align images[44]. We used a discrete Fourier transform based method that calculated shifts with sub-pixel increments. A registration template was constructed from averaging the first 10–100 images collected, or 10–100 images that had the lowest luminance value; both methods resulted in similarly stable images. Each image was aligned to the template. Mean and standard deviation projections of the registered stack were made, from which somatic regions of interests (ROIs) were made using semi-automated segmentation of factors found using non-negative matrix factorization. All ROIs were inspected manually. A binary mask from the segmented regions was made for later processing. Fluorescence values were extracted from each ROI for each frame, and the mean for each cell was computed. In addition, we made annulus-shaped ROIs to estimate neuropil contamination by eroding out 15 pixels from each somatic ROI and subtracting any other cell body that fell in this ring. This gave us two vectors of fluorescence values for the soma and the neuropil. We weighted the neuropil vector by 0.8, which was on the high side of contamination estimates we made by comparing the difference in blood vessels and their surround[45]. The weighted neuropil vector was subtracted from the somatic vector to produce a corrected vector of fluorescence values.

Fluorescence value (F) traces were converted to a normalized F/F trace. We used an approach similar to previous population calcium imaging studies to estimate baseline F_0 fluorescence in each cell. F_0 computed via a sliding-window of 500 frames (approximately 50 seconds) using a quartile cut-off that ranged from the bottom tenth percentile up to the median, depending on how active the neuron was[46]. Lastly, F and F_0 traces were used to make the final F/F trace given by $(F(i)-F_0(i))/F_0(i)$, where i is the index for each frame. Records of F/F were grouped into trials and aligned to stimulus onsets for behavioral data for further analysis. We excluded neurons with filled nuclei, which we determined during segmentation by looking at time-lapse movies as well as average and variance projection images. We also looked for disproportionately long decay-time for spontaneous transients as an indication of filled neurons. These neurons comprised at most 1.5% of our imaging fields.

We defined stimulus responsive neurons as those whose evoked-GCaMP6 F/F values (the magnitude of F/F integrated over 500 ms post-stimulus minus the baseline F/F integrated over 500 ms pre-stimulus), averaged across trials with 0.75–1.00 mm deflection amplitudes (the higher end of the detectable range), differed significantly ($p<0.05$; bootstrap mean-difference test) than evoked activity averaged across trials with a zero-amplitude stimulus.

We estimated event-rate by counting the total number of deconvolved events from the resulting F/F traces using a robust non-negative deconvolution method[47,48] implemented in MATLAB (https://github.com/zhoupc/OASIS_matlab). Event rate was defined as the number of individual Ca^{2+}-transients discharged in a ten-minute period. The algorithm has few hand-tunable parameters, but it takes a "Noise Factor" for thresholding noise and signal during its pre-processing steps. We empirically determined this factor for excitatory and inhibitory cells separately and found that a factor of 1 for excitatory cells and 5 for inhibitory cells to result in 'de-noised' F/F traces that were closest to visually inspect raw data. We swept the range of noise factors for all neurons analyzed and computed the R^2 value between raw data and the algorithm's processed data and observed that R^2 peaked at 0.99 at our chosen noise factor values, but were largely stable over a wide range of values.

Correlation coefficients were computed as the Spearman's rank correlation coefficient (ρ) using the built-in MATLAB 'corr' function. To construct distributions of correlations in spontaneous activity, we computed ρ for all possible pairings of neurons deemed active at all (showed at least ten calcium-events in ten minutes, e.g. rate > 0.01 Hz), for all of an experimental group's spontaneous firing imaging sessions, which were then pooled. *p*-values for ρ were determined using the same Matlab function, which computes the tail-probability of the Spearman 'D-statistic'.

Peri-stimulus time histograms (PSTHs) were made by determining the average evoked-response across six different amplitudes of whisker deflections, including the zero-amplitude stimuli. We did this for all stimulus responsive neurons and converted F/F to standard scores (Z-scores), which allowed us to determine the degree to which the magnitude of evoked-responses differed between WT and *Shank3B*$^{-/-}$ mice despite differences in their baseline spontaneous activity.

In Vitro Electrophysiology and single cell genotyping

Slice preparation—The slice preparations were followed by previously described. Briefly, the mice injected with AAV$_{2/8}$-CaMKII-GCaMP6 and AAV$_{2/8}$-Dlx5/6-Cre-mKate2 were anesthetized via isoflurane and transcardially perfused with 20 ml of ice-cold carbogenated (95% O2 and 5% CO2,) cutting solution containing (in mM): 194 sucrose, 30 NaCl, 4.5 KCl, 1.2 NaH2PO4, 0.2 CaCl2, 2 MgCl2, 26 NaHCO3, and 10 D-(+)-glucose (with osmolarity of 300–305 mOsm/l). The brain was rapidly removed and placed into ice-cold cutting solution for slice preparation. The coronal slices (300 μm) containing the somatosensory cortex were prepared by a slicer (VT1200S, Leica, Germany) and then incubated in a holding chamber at 32 °C for 15–20 min. Then the slices were transferred to artificial cerebral spinal fluid containing (in mM): 136 NaCl, 3.5 KCl, 1 MgCl2, 2.5 CaCl2, 26 NaHCO3 and 11 glucose (with osmolarity of 295–300 mOsm/l) at room temperature for at least 1h.

Electrophysiological recordings—Whole-cell patch clamp recordings were performed with infrared differential interference contrast visualization at room temperature (21–25 °C). The fluorescently labeled neurons were visualized and identified with a microscope equipped with GCaMP6 or red fluorescent protein (mKate2) filter (BX-51WI, Olympus).

Recording pipettes (BF150–86-7.5, Sutter Instruments) were pulled in a horizontal pipette puller (P-97, Sutter Instruments) with a tip resistance of 3–5 MΩ. Patch pipettes were filled with a solution containing (in mM): 128 potassium gluconate, 10 Hepes, 10 phosphocreatine sodium salt, 1.1 EGTA, 5 ATP magnesium salt, and 0.4 GTP sodium salt. pH was adjusted to 7.3 with KOH, and osmolarity was adjusted to 300–305 mOsm with sucrose. An axon 700B amplifier (Molecular Devices) was used to record membrane potentials. Signals were low-pass filtered at 5 kHz and sampled at 20 kHz with a Digidata 1550 and Clampex 10.6 (Molecular Devices), and data were stored on a computer for subsequent off-line analysis.

Single cell collection and PCR—To collect intact single cell and minimal the contamination, we cleaned all work surfaces and equipment with DNA-OFF (Takara Cat. #9036). Pipettes of 2–4 MΩ resistance were filled with intracellular solution (the same recipe with electrorheological recordings). We gave a positive pressure before attaching the cell. When the pipette touching the neuron, we removed the positive pressure immediately and applied light suction until the cell had visibly clung to the tip of pipette. Then pick up the cell slowly and gently under the guidance of microscope, seeing the detachment of the cell from the slice. After that, we broke the tip of the pipette in the PCR tube containing 4 ul of 1X PBS buffer and snap frozen on dry ice. The samples were transferred to −80°C until further processing. According to the recommended protocols single-cell gDNA samples were amplified by REPLI-g Single Cell Kit (Qiagen). Briefly, the single cell solution was taken out from −80°C and added 3 ul of Buffer D2. Samples were incubated for 10 min at 65°C and the reaction was stopped by adding of 3 ul of Stop buffer. Samples were incubated for another 10 hs at 30°C after adding the amplification mix (29 μl buffer, 2 μl REPLI sc DNA polymerase) and at 65°C for 10 min. After amplification, the products were used for PCR analysis. The PCR primers are: F1: 5'-CAGCATTTATACCTGACTGTGAAGC-3', R1: 5' -GGGAGTAGAGCTCAGATAACC-3' and R2: 5'-CTTTGTAAGACCAAAGTGTGG-3'. And the PCR amplification condition is: 95°C for 5 min, 95°C ,30s; 58°C ,30s; 58°C ,60s; for 35 cycles, 72°C for 5 min. The PCR products were running on 2% agarose gels.

Statistics

All comparisons between groups were collected from littermate animals with experiments performed at the same time. No statistical methods were used to predetermine sample sizes, but our sample sizes are similar to those reported in previous publications[9,12]. With few exceptions, hypothesis testing between two groups using a bootstrap mean-difference test that does not assume the underlying data are normally distributed. For these tests, we computed a bootstrap distribution of the difference in the two group's means, for each of 10,000 permutations. Normality of the resulting bootstrap distribution was determined by comparing it to a randomly sampled normal distribution with the same mean and standard deviation as the bootstrap distribution. We used the confidence intervals of the resulting bootstrap distribution to derive p-values[49]. We report all p-values greater than 0.0001 as the actual p-value, but those less than 0.0001 are reported as $p<0.0001$. Throughout the study, we used $p<0.05$ as threshold for rejecting the null-hypothesis. Calculation of the statistics was done in MATLAB2018b (Mathworks). Further details on particular statistical analyses can be found on the respective figures/results section for each dataset. In two experiments we performed a two-tailed, unpaired, Student's t-test using Prism 7 (GraphPad Software,

Inc.), for those experiments we did not formally test for normality and equal variance, but assumed the data were normally distributed and had equal variance. In those two cases, we show the underlying data points or distribution. Experiments were randomized and the investigators were blind to the genotypes during the experiments and outcome assessment.

Supplementary Material

Refer to Web version on PubMed Central for supplementary material.

Acknowledgements

References

1. Amso D, Haas S, Tenenbaum E, Markant J & Sheinkopf SJ. Bottom-up attention orienting in young children with autism. Journal of autism and developmental disorders 44, 664–673, doi:10.1007/s10803-013-1925-5 (2014). [PubMed: 23996226]

2. Leekam SR, Nieto C, Libby SJ, Wing L & Gould J. Describing the sensory abnormalities of children and adults with autism. Journal of autism and developmental disorders 37, 894–910, doi:10.1007/s10803-006-0218-7 (2007). [PubMed: 17016677]

3. Wang AT. et al. Neural selectivity for communicative auditory signals in Phelan-McDermid syndrome. Journal of neurodevelopmental disorders 8, 5, doi:10.1186/s11689-016-9138-9 (2016). [PubMed: 26909118]

4. Gogolla N, Takesian AE, Feng G, Fagiolini M & Hensch TK. Sensory integration in mouse insular cortex reflects GABA circuit maturation. Neuron 83, 894–905, doi:10.1016/j.neuron.2014.06.033 (2014). [PubMed: 25088363]

5. Goncalves JT, Anstey JE, Golshani P & Portera-Cailliau C. Circuit level defects in the developing neocortex of Fragile X mice. Nature neuroscience 16, 903–909, doi:10.1038/nn.3415 (2013). [PubMed: 23727819]

6. Chao HT. et al. Dysfunction in GABA signalling mediates autism-like stereotypies and Rett syndrome phenotypes. Nature 468, 263–269, doi:10.1038/nature09582 (2010). [PubMed: 21068835]

7. Zhang Y. et al. Dendritic channelopathies contribute to neocortical and sensory hyperexcitability in Fmr1(-/y) mice. Nature neuroscience 17, 1701–1709, doi:10.1038/nn.3864 (2014). [PubMed: 25383903]

8. Orefice LL. et al. Peripheral Mechanosensory Neuron Dysfunction Underlies Tactile and Behavioral Deficits in Mouse Models of ASDs. Cell 166, 299–313, doi:10.1016/j.cell.2016.05.033 (2016). [PubMed: 27293187]

9. Peca J. et al. Shank3 mutant mice display autistic-like behaviours and striatal dysfunction. Nature 472, 437–442, doi:10.1038/nature09965 (2011). [PubMed: 21423165]

10. Naisbitt S. et al. Shank, a novel family of postsynaptic density proteins that binds to the NMDA receptor/PSD-95/GKAP complex and cortactin. Neuron 23, 569–582 (1999). [PubMed: 10433268]

11. Bozdagi O. et al. Haploinsufficiency of the autism-associated Shank3 gene leads to deficits in synaptic function, social interaction, and social communication. Molecular autism 1, 15, doi:10.1186/2040-2392-1-15 (2010). [PubMed: 21167025]

12. Mei Y. et al. Adult restoration of Shank3 expression rescues selective autistic-like phenotypes. Nature 530, 481–484, doi:10.1038/nature16971 (2016). [PubMed: 26886798]

13. Wang X. et al. Altered mGluR5-Homer scaffolds and corticostriatal connectivity in a Shank3 complete knockout model of autism. Nature communications 7, 11459, doi:10.1038/ncomms11459 (2016).

14. Wang X. et al. Synaptic dysfunction and abnormal behaviors in mice lacking major isoforms of Shank3. Human molecular genetics 20, 3093–3108, doi:10.1093/hmg/ddr212 (2011). [PubMed: 21558424]

15. Siegle JH, Pritchett DL & Moore CI. Gamma-range synchronization of fast-spiking interneurons can enhance detection of tactile stimuli. Nature neuroscience 17, 1371–1379, doi:10.1038/nn.3797 (2014). [PubMed: 25151266]

16. Luo TZ & Maunsell JH. Neuronal Modulations in Visual Cortex Are Associated with Only One of Multiple Components of Attention. Neuron 86, 1182–1188, doi:10.1016/j.neuron.2015.05.007 (2015). [PubMed: 26050038]

17. Goel A. et al. Impaired perceptual learning in a mouse model of Fragile X syndrome is mediated by parvalbumin neuron dysfunction and is reversible. Nature neuroscience 21, 1404–1411, doi:10.1038/s41593-018-0231-0 (2018). [PubMed: 30250263]

18. de la Rocha J, Doiron B, Shea-Brown E, Josic K & Reyes A. Correlation between neural spike trains increases with firing rate. Nature 448, 802–806, doi:10.1038/nature06028 (2007). [PubMed: 17700699]

19. Chen TW. et al. Ultrasensitive fluorescent proteins for imaging neuronal activity. Nature 499, 295–300, doi:10.1038/nature12354 (2013). [PubMed: 23868258]

20. Doiron B, Litwin-Kumar A, Rosenbaum R, Ocker GK & Josic K. The mechanics of state-dependent neural correlations. Nature neuroscience 19, 383–393, doi:10.1038/nn.4242 (2016). [PubMed: 26906505]

21. Peron SP, Freeman J, Iyer V, Guo C & Svoboda K. A Cellular Resolution Map of Barrel Cortex Activity during Tactile Behavior. Neuron 86, 783–799, doi:10.1016/j.neuron.2015.03.027 (2015). [PubMed: 25913859]

22. Crochet S, Poulet JF, Kremer Y & Petersen CC. Synaptic mechanisms underlying sparse coding of active touch. Neuron 69, 1160–1175, doi:10.1016/j.neuron.2011.02.022 (2011). [PubMed: 21435560]

23. Yang H, Kwon SE, Severson KS & O'Connor DH. Origins of choice-related activity in mouse somatosensory cortex. Nature neuroscience 19, 127–134, doi:10.1038/nn.4183 (2016). [PubMed: 26642088]

24. Kim E & Sheng M. PDZ domain proteins of synapses. Nature reviews. Neuroscience 5, 771–781, doi:10.1038/nrn1517 (2004). [PubMed: 15378037]

25. Kouser M. et al. Loss of predominant Shank3 isoforms results in hippocampus-dependent impairments in behavior and synaptic transmission. The Journal of neuroscience : the official journal of the Society for Neuroscience 33, 18448–18468, doi:10.1523/JNEUROSCI.3017-13.2013 (2013). [PubMed: 24259569]

26. Cruikshank SJ. et al. Thalamic control of layer 1 circuits in prefrontal cortex. The Journal of neuroscience : the official journal of the Society for Neuroscience 32, 17813–17823, doi:10.1523/JNEUROSCI.3231-12.2012 (2012). [PubMed: 23223300]

27. Moore CI & Nelson SB. Spatio-temporal subthreshold receptive fields in the vibrissa representation of rat primary somatosensory cortex. Journal of neurophysiology 80, 2882–2892 (1998). [PubMed: 9862892]

28. Wehr M & Zador AM. Balanced inhibition underlies tuning and sharpens spike timing in auditory cortex. Nature 426, 442–446, doi:10.1038/nature02116 (2003). [PubMed: 14647382]

29. Orefice LL. et al. Targeting Peripheral Somatosensory Neurons to Improve Tactile-Related Phenotypes in ASD Models. Cell 178, 867–886 e824, doi:10.1016/j.cell.2019.07.024 (2019). [PubMed: 31398341]

30. Dimidschstein J. et al. A viral strategy for targeting and manipulating interneurons across vertebrate species. Nature neuroscience 19, 1743–1749, doi:10.1038/nn.4430 (2016). [PubMed: 27798629]

31. Sachidhanandam S, Sermet BS & Petersen CCH. Parvalbumin-Expressing GABAergic Neurons in Mouse Barrel Cortex Contribute to Gating a Goal-Directed Sensorimotor Transformation. Cell reports 15, 700–706, doi:10.1016/j.celrep.2016.03.063 (2016). [PubMed: 27149853]

32. Goffin D, Brodkin ES, Blendy JA, Siegel SJ & Zhou Z. Cellular origins of auditory event-related potential deficits in Rett syndrome. Nature neuroscience 17, 804–806, doi:10.1038/nn.3710 (2014). [PubMed: 24777420]

33. Selby L, Zhang C & Sun QQ. Major defects in neocortical GABAergic inhibitory circuits in mice lacking the fragile X mental retardation protein. Neuroscience letters 412, 227–232, doi:10.1016/j.neulet.2006.11.062 (2007). [PubMed: 17197085]

34. O'Neill M & Jones RS. Sensory-perceptual abnormalities in autism: a case for more research? Journal of autism and developmental disorders 27, 283–293 (1997). [PubMed: 9229259]

35. Marco EJ, Hinkley LB, Hill SS & Nagarajan SS. Sensory processing in autism: a review of neurophysiologic findings. Pediatric research 69, 48R–54R, doi:10.1203/PDR.0b013e3182130c54 (2011).

36. Lee J. et al. Shank3-mutant mice lacking exon 9 show altered excitation/inhibition balance, enhanced rearing, and spatial memory deficit. Frontiers in cellular neuroscience 9, 94, doi:10.3389/fncel.2015.00094 (2015). [PubMed: 25852484]

37. Tu JC. et al. Coupling of mGluR/Homer and PSD-95 complexes by the Shank family of postsynaptic density proteins. Neuron 23, 583–592 (1999). [PubMed: 10433269]

38. Peixoto RT, Wang W, Croney DM, Kozorovitskiy Y & Sabatini BL. Early hyperactivity and precocious maturation of corticostriatal circuits in Shank3B(−/−) mice. Nature neuroscience 19, 716–724, doi:10.1038/nn.4260 (2016). [PubMed: 26928064]

39. Rubenstein JL & Merzenich MM. Model of autism: increased ratio of excitation/inhibition in key neural systems. Genes, brain, and behavior 2, 255–267 (2003).

40. Bolton PF. et al. Epilepsy in autism: features and correlates. The British journal of psychiatry : the journal of mental science 198, 289–294, doi:10.1192/bjp.bp.109.076877 (2011). [PubMed: 21972278]

Methods-only References

41. Thompson KJ. et al. DREADD Agonist 21 Is an Effective Agonist for Muscarinic-Based DREADDs in Vitro and in Vivo. ACS pharmacology & translational science 1, 61–72, doi:10.1021/acsptsci.8b00012 (2018). [PubMed: 30868140]

42. Chen Q. et al. Imaging neural activity using Thy1-GCaMP transgenic mice. Neuron 76, 297–308, doi:10.1016/j.neuron.2012.07.011 (2012). [PubMed: 23083733]

43. Truszkowski TL. et al. A cellular mechanism for inverse effectiveness in multisensory integration. eLife 6, doi:10.7554/eLife.25392 (2017).

44. Guizar-Sicairos M, Thurman ST & Fienup JR. Efficient subpixel image registration algorithms. Optics letters 33, 156–158 (2008). [PubMed: 18197224]

45. Kerlin AM, Andermann ML, Berezovskii VK & Reid RC. Broadly tuned response properties of diverse inhibitory neuron subtypes in mouse visual cortex. Neuron 67, 858–871, doi:10.1016/j.neuron.2010.08.002 (2010). [PubMed: 20826316]

46. Komiyama T. et al. Learning-related fine-scale specificity imaged in motor cortex circuits of behaving mice. Nature 464, 1182–1186, doi:10.1038/nature08897 (2010). [PubMed: 20376005]

47. Pachitariu M, Stringer C & Harris KD. Robustness of Spike Deconvolution for Neuronal Calcium Imaging. The Journal of neuroscience : the official journal of the Society for Neuroscience 38, 7976–7985, doi:10.1523/JNEUROSCI.3339-17.2018 (2018). [PubMed: 30082416]

48. Friedrich J, Zhou P & Paninski L. Fast online deconvolution of calcium imaging data. PLoS computational biology 13, e1005423, doi:10.1371/journal.pcbi.1005423 (2017). [PubMed: 28291787]

49. Altman DG & Bland JM. How to obtain the confidence interval from a P value. Bmj 343, d2090, doi:10.1136/bmj.d2090 (2011). [PubMed: 21824904]
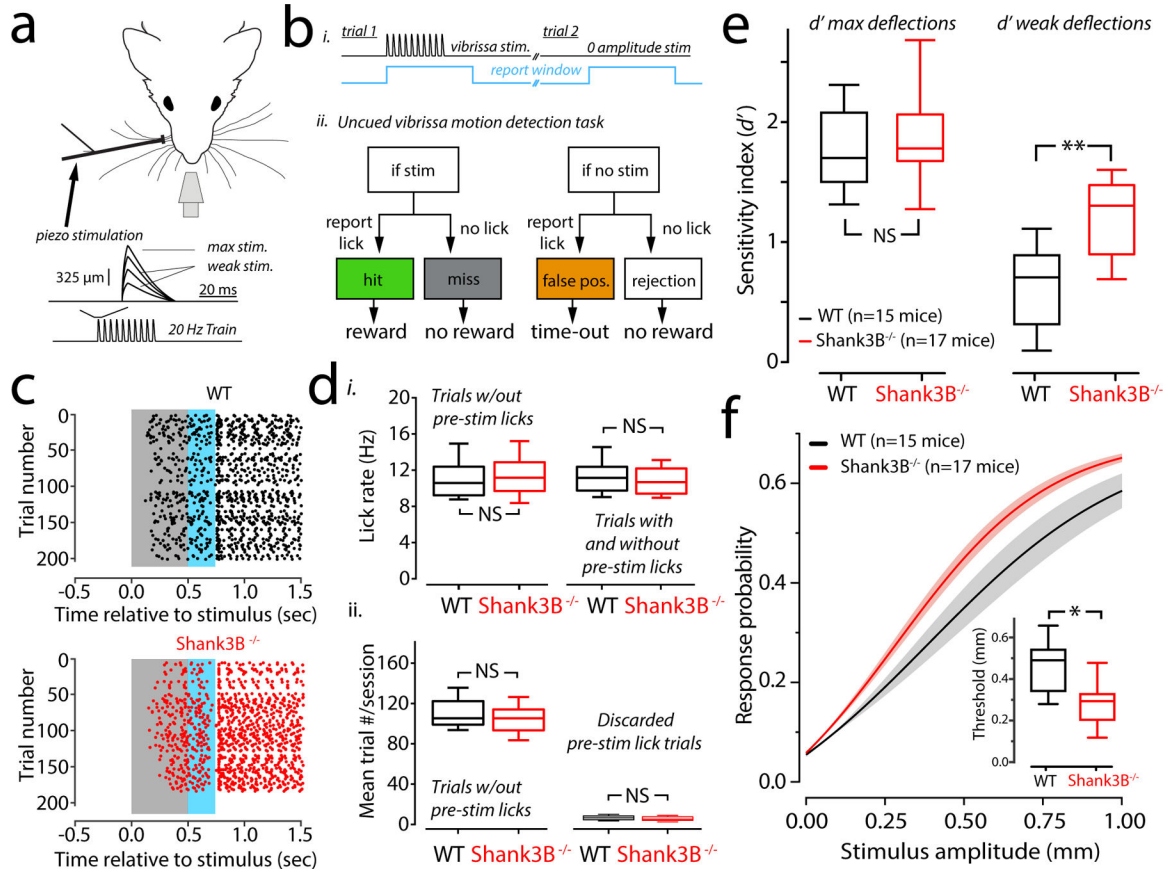
Figure 1. Vibrissa detection and stimulus hyper-reactivity in *Shank3B*⁻/⁻ mice.

(**a**) Head-restrained mice were trained to lick at a waterspout when they detected vibrissa motion delivered via a piezo. The blow-up shows the shape of an individual deflection, which had a variable amplitude from trial-to-trial. (**b**) *i*) Trials in the task consisted of a variable inter-trial interval (1–6.5 seconds) after which a stimulus was presented (black trace), which coincided with the triggering of a 'report window' (blue). *ii*) Flow chart of the task. (**c**) Example lick of a WT (top, black dots) and *Shank3B*⁻/⁻ (bottom, red dots) in the late stage of training. Each dot represents a lick. These lick rasters show the distribution of individual licks as dots in a given trial relative to stimulus onset. (**d**) *i*, Box-plots of mean lick rates for WT (black; n=10 mice) and *Shank3B*⁻/⁻ (red; n=10 mice) animals. *Left*, shows average lick rate for trials analyzed further in the study that showed no pre-stimulus licking. *Right*, average lick rate but including all the trials discarded due to pre-stimulus licking. In either case, there was no significant difference in lick rates (*p*=0.7& *p*=0.8; bootstrap mean-difference test). *ii*, Left, Box-plots showing the average number of trials per session completed by WT (black) and *Shank3B*⁻/⁻ (red) mice. Right, same as left, but the average number of trials that were discarded per session because of pre-stimulus licking. There was no significant difference between WT and *Shank3B*⁻/⁻ groups for either comparison (*p*=0.8, left & *p*=0.6, right; bootstrap mean-difference test). (**e**) Box-plots showing the sample distributions of the detection sensitivity (*d'*) for strong (left) and weak (right) stimuli. Left, there was no statistical difference in the *d'* for strong (1 mm) whisker deflections (WT mean ± s.e.m.: 1.79 ± 0.10; black; *Shank3B*⁻/⁻ mean ± s.e.m.: 1.8 ±0.11, red; n=15 WT, n=17

Shank3B$^{-/-}$; *p*=0.53; bootstrap mean-difference test). Right, *Shank3B*$^{-/-}$ mice have a significantly higher *d'* for weak stimuli (WT mean ± s.e.m.: 0.59 ± 0.10; *Shank3B*$^{-/-}$ mean ± s.e.m.: 1.2 ± 0.09; n=15 WT, black; n=17 *Shank3B*$^{-/-}$ mice, red; ***p<0.0001; bootstrap mean-difference test). (**f**) Mean psychometric curves (sigmoidal function fits) from the sessions used in *e*. Solid lines denote the mean, and the shaded regions are the standard error of the mean. The inset show a significant difference of detection threshold between groups (WT mean ± s.e.m.: 449 ± 42 μm; *Shank3B*$^{-/-}$ mean ± s.e.m.: 296 ± 43 μm; n=15 WT mice and 17 *Shank3B*$^{-/-}$ mice; **p=0.003; bootstrap mean-difference test;). There was also a difference in the unitless slope-factor (WT mean ± s.e.m.: 232 ± 17 μm; *Shank3B*$^{-/-}$ mean ± s.e.m.: 149 ± 18 μm, n=15 WT mice and 17 *Shank3B*$^{-/-}$ mice; *p*<0.0001, bootstrap mean-difference test), which is a fit parameter related to how steep the curve is. Box-and-whisker plots show median values (middle vertical bar) and 25th (bottom side of the box) and 75th percentiles (top side of the box) with whiskers indicating the range. All bootstrap mean-difference tests were two-sided. These results repeated three times.
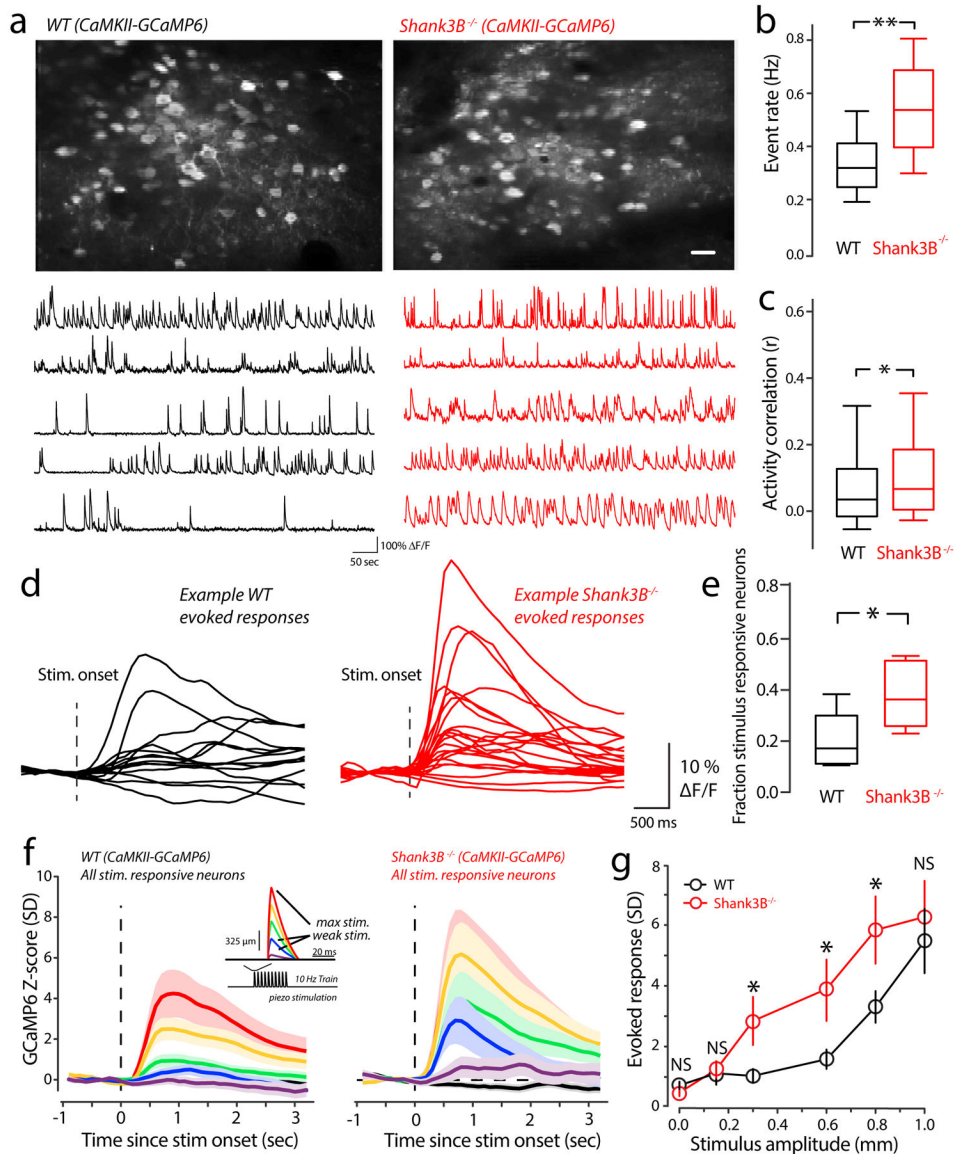
Figure 2. Enhanced spontaneous and stimulus-evoked activity in *Shank3B*$^{-/-}$ excitatory neurons.
(**a**) Upper panels: example mean two-photon CaMKII-GCaMP6 imaging fields from a WT
(left) and *Shank3B*$^{-/-}$ (right) mouse. Scale bar is 50 μm. Lower panels: example
spontaneous F/F time-series traces from the upper imaging fields from WT (left) and
Shank3B$^{-/-}$ (right) mouse. (**b**) Box-plots quantifying differences of spontaneous calcium
event rate that was determined by counting the total number of deconvolved individual Ca^{2+}-
events for ten minutes (n=612 neurons from 6 WT mice; 653 neurons from 6 *Shank3B*$^{-/-}$
mice). Asterisk denotes a statistically significant difference between the sample groups
(**p<0.0001; bootstrap mean-difference test). (**c**) The correlation between spontaneous
firing was quantified as the Spearman's rank correlation coefficient (ρ). Box-plots show the
distribution of all pooled correlations between WT and *Shank3B*$^{-/-}$ excitatory neurons
(n=65,931 pairs from 6 WT mice; n=65,092 pairs from 6 *Shank3B*$^{-/-}$ mice), and show an
overall increase in correlations among excitatory neurons in *Shank3B*$^{-/-}$ compared to WT.

Asterisk denotes a statistically-significant difference between the sample groups (*p=0.004; bootstrap mean-difference test). (**d**) Example traces showing the F/F responses to maximal (1mm) whisker deflections stimulus of the responsive neurons from a representative WT (black) and *Shank3B*$^{-/-}$ (red) mice. The dashed line indicates the onset of the whisker stimulus. (**e**) Box-plots showing the fraction of neurons determined to be stimulus responsive in WT (black; n=6) and *Shank3B*$^{-/-}$ (red; n=6) mice. Asterisk denotes a statistically significant difference between the sample groups (*p=0.002; bootstrap mean-difference test). (**f**) Left panel: The magnitude of evoked responses in WT mice, across the range of stimulus amplitudes. We quantified this by constructing peri-stimulus time histograms (PSTHs) from Z-scored evoked-responses for all of the responsive neurons (n=107 from 6 WT mice, n=93 from 6 *Shank3B*$^{-/-}$ mice). The average response for each stimulus amplitude is color coded as indicated by the inset showing the piezo-stimulus waveform (red is the maximal deflection; purple is the weakest). Line on all plots indicate the mean and the shaded regions corresponds to the standard error of the mean. Right panel: same as in *left panel*, but from *Shank3B*$^{-/-}$ mice. (**g**) Comparison of peak-evoked responses across the stimulus-amplitudes tested for responsive neurons (n=107 from 6 WT mice (black), n=93 from 6 *Shank3B*$^{-/-}$ mice (red). The center of the circles represents the mean and the error bars represent to the standard error of the mean. Asterisks denote statistically significant differences (n=107 from 6 WT mice; n=93 from 6 *Shank3B*$^{-/-}$ mice, *p<0.05, NS denotes no difference p>0.05; bootstrap mean-difference test), p-values in order from left-to-right: 0.24, 0.75, 0.03, 0.03, 0.04, 0.75). These results repeated three times. Box-and-whisker plots show median values (middle vertical bar) and 25th (bottom side of the box) and 75th percentiles (top side of the box) with whiskers indicating the range. All bootstrap mean-difference tests were two-sided.
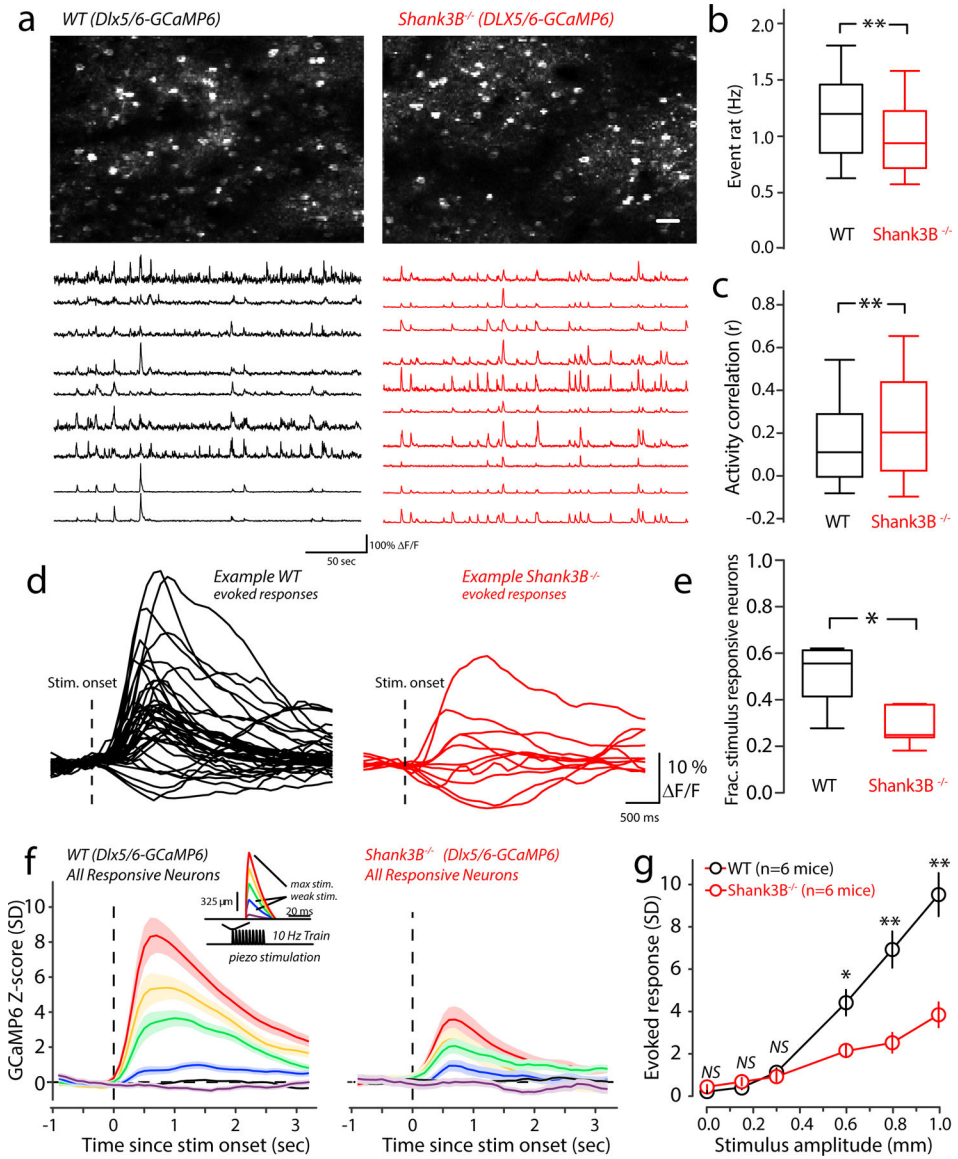
Figure 3. Reduced spontaneous and stimulus-evoked activity in *Shank3B*^−/− inhibitory neurons.
(**a**) Upper panels: example mean two-photon Dlx5/6-GCaMP6 imaging fields from a WT
(left) and *Shank3B*^−/− (right) mouse. Scale bar is 50 μm. Lower panels: example
spontaneous ΔF/F time-series traces from the upper imaging fields from WT (left) and
Shank3B^−/− (right) mouse. (**b**) Box-plots quantifying differences of spontaneous calcium
event rate that was determined by counting the total number of deconvolved individual Ca^{2+}-
events for ten minutes (n=382 neurons from 6 WT mice; 402 neurons from 6 *Shank3B*^−/−
mice). Asterisk denotes a statistically significant difference between the sample groups
(**p<0.0001; bootstrap-mean-difference test). (**c**) The correlation between spontaneous
firing was quantified as the Spearman's rank correlation coefficient (ρ) for all possible
pairings in each imaging session, and then pooled across sessions. Box-plots show the
distribution of all pooled correlations between WT and *Shank3B*^−/− inhibitory neurons
(n=39,018 pairs from 6 WT mice; 43,954 pairs from 6 *Shank3B*^−/− mice), and show an

overall increase in correlations among inhibitory neurons in *Shank3B*$^{-/-}$ compared to WT. Asterisk denotes a statistically significant difference between the sample groups (**p<0.0001; bootstrap mean-difference test). (**d**) Example traces showing the F/F responses to maximal (1mm) whisker deflections stimulus of the responsive neurons from a representative WT (black) and *Shank3B*$^{-/-}$ (red) mice. The dashed line indicates the onset of the whisker stimulus. (**e**) Box-plots showing the fraction of neurons determined to be stimulus responsive in WT (black; n=6) and *Shank3B*$^{-/-}$ (red; n=6) mice. Asterisk denotes a statistically significant difference between the sample groups (; mean proportion WT =0.58 ± 0.05, n= 6 mice; mean proportion *Shank3B*$^{-/-}$ = 0.28 ± 0.06, n= 6 mice; *p=0.0002; bootstrap mean-difference test). (**f**) Left panel: The magnitude of evoked responses in WT mice, across the range of stimulus amplitudes. We quantified this by constructing peri-stimulus time histograms (PSTHs) from Z-scored evoked-responses for all of the responsive neurons (n=237 from 6 WT mice, n=114 from 6 *Shank3B*$^{-/-}$ mice). The average response for each stimulus amplitude is color coded as indicated by the inset showing the piezo-stimulus waveform (red is the maximal deflection; purple is the weakest). Line indicates the mean and the shaded region corresponds to the standard error of the mean. Right panel: same as in *left panel*, but from *Shank3B*$^{-/-}$ mice. (**g**) Comparison of peak-evoked responses across the stimulus-amplitudes tested for WT (black) and *Shank3B*$^{-/-}$ (red) mice, (n=237 from 6 WT mice, n=114 from 6 *Shank3B*$^{-/-}$ mice). Center of circles represent the mean and the error bars indicate the standard error of the mean, asterisks denote statistically significant differences (NS denotes no difference p>0.05; *p<0.05, **p<0.0001, bootstrap mean-difference test, p-values in order from left-to-right: 0.5, 0.6, 0.9, 0.001, <0.0001, <0.0001. These results repeated three times. Box-and-whisker plots show median values (middle vertical bar) and 25th (bottom side of the box) and 75th percentiles (top side of the box) with whiskers indicating the range. All bootstrap mean-difference tests were two-sided.
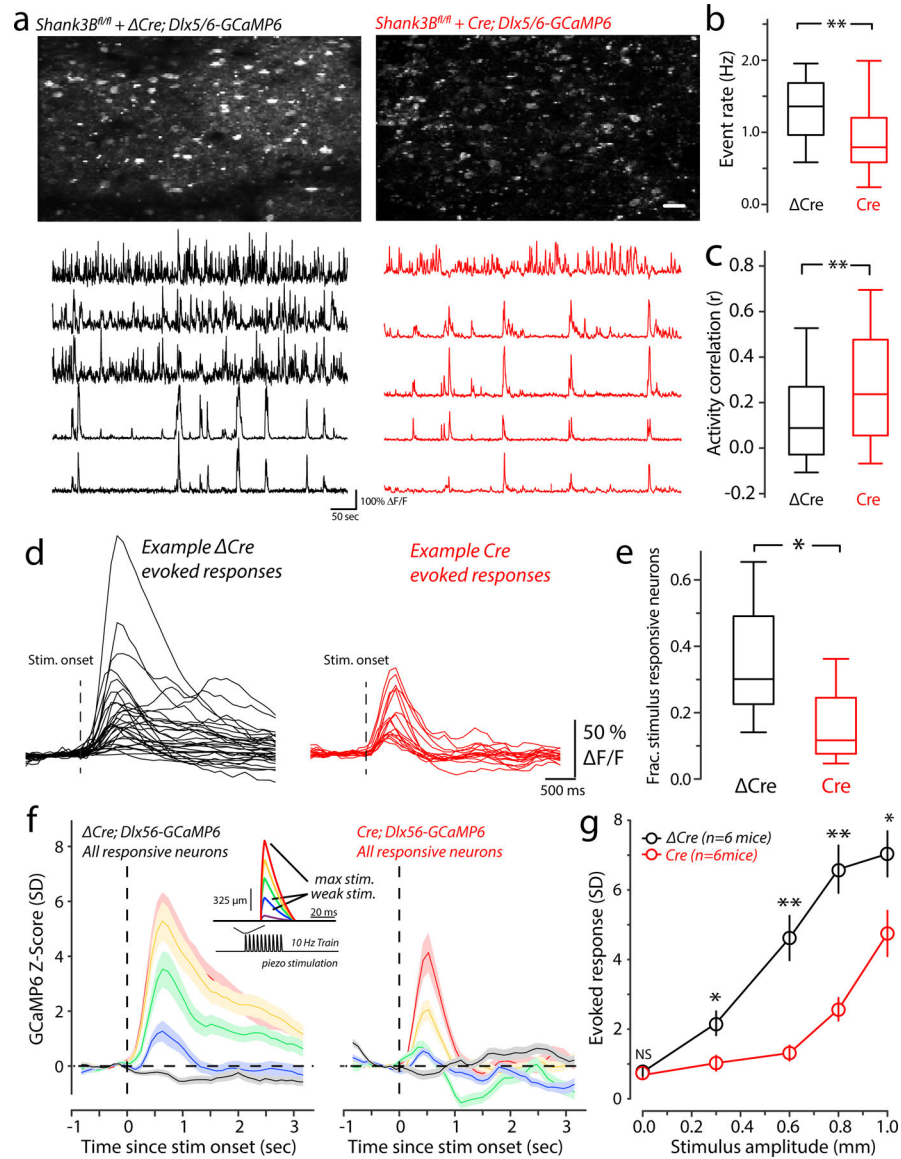
Figure 4. Reduced spontaneous and stimulus-evoked activity in inhibitory neurons after preferential deletion of *Shank3* in interneurons in vS1.
(**a**) Upper panels: example mean two-photon Dlx5/6-GCaMP6 imaging fields from an AAV-Dlx5/6- Cre-mKate2-injected (left) and AAV-Dlx5/6-Cre-mKate2-injected (right) *Shank3B*^fl/fl mouse. Scale bar is 50 μm. Lower panels: example spontaneous F/F time-series traces from the upper imaging fields from Dlx5/6- Cre-injected (left) and Dlx5/6-Cre-injected (right) Shank.*3B*^fl/fl mouse. (**b**) Box-plots quantifying differences of spontaneous calcium event rate that was determined by counting the total number of deconvolved individual Ca^{2+}-events for ten minutes (n=432 neurons from 6 Dlx5/6- Cre-injected mice; 407 neurons from 6 Dlx5/6-Cre-injected mice). Asterisk denotes a statistically significant difference between the sample groups (**p<0.0001; bootstrap mean-difference test). (**c**) The correlation between spontaneous firing was quantified as the Spearman's rank correlation coefficient (ρ) for all possible pairings in each imaging session, and then pooled across sessions. Box-plots show the distribution of all pooled correlations

between Dlx5/6- Cre-injected (control group) and Dlx5/6-Cre-injected (local knock-out group) inhibitory neurons (n=37,464 pairs from 6 Dlx5/6- Cre-injected mice; n=35,372 pairs from 6 Dlx5/6-Cre-injected mice), and show an overall increase in correlations among inhibitory neurons in Dlx5/6-Cre-injected compared to Dlx5/6- Cre-injected. Asterisk denotes a statistically significant difference between the sample groups (**p<0.0001; bootstrap mean-difference test). (**d**) Example traces showing the F/F responses to maximal (1mm) whisker deflections stimulus of the responsive neurons from a representative Dlx5/6- Cre-injected (black) and Dlx5/6-Cre-injected (red) mice. The dashed line indicates the onset of the whisker stimulus. (**e**) Box-plots showing the fraction of neurons determined to be stimulus responsive neurons in Dlx5/6- Cre-injected (black; n=6) and Dlx5/6-Cre-injected (red; n=6) mice. Asterisk denotes a statistically significant difference between the sample groups (Dlx5/6- Cre group proportion = 0.39 ± 0.09, n=6 mice; Dlx5/6-Cre group proportion = 0.16 ± 0.05, n=6 mice; mean ± s.e.m.; *p=0.01; bootstrap mean-difference test). (**f**) Left panel: The magnitude of evoked responses in Dlx5/6- Cre-injected mice, across the range of stimulus amplitudes was quantified by constructing peri-stimulus time histograms (PSTHs) from Z-scored evoked-responses for all of the responsive neurons (n=102 from 6 Dlx5/6- Cre mice, n=58 from 6 Dlx5/6-Cre mice). The average response for each stimulus amplitude is color coded as indicated by the inset showing the piezo-stimulus waveform (red is the maximal deflection, purple is the weakest). Line on all plots indicate the mean and the shaded regions corresponds to the standard error of the mean. Right panel: same as in *left panel*, but from Dlx5/6- Cre-injected. (**g**) Comparison of peak-evoked responses across the stimulus-amplitudes tested for Dlx5/6- Cre-injected (black) and Dlx5/6-Cre-injected (red) mice (n=102 from 6 Dlx5/6- Cre mice, n=58 from 6 Dlx5/6-Cre mice). Asterisks denote statistically significant differences (*p<0.05, **p<0.0001, NS denotes no *p*>0.05; bootstrap mean-difference test, *p*-values in order from left-to-right: 0.4, 0.003, <0.0001, <0.0001 and 0.03). Box-and-whisker plots show median values (middle vertical bar) and 25th (bottom side of the box) and 75th percentiles (top side of the box) with whiskers indicating the range. All bootstrap mean-difference tests were two-sided. Cre: AAV-Dlx5/6- Cre-mKate2-injected mouse group; Cre: AAV-Dlx5/6-Cre-mKate2-injected mouse group.
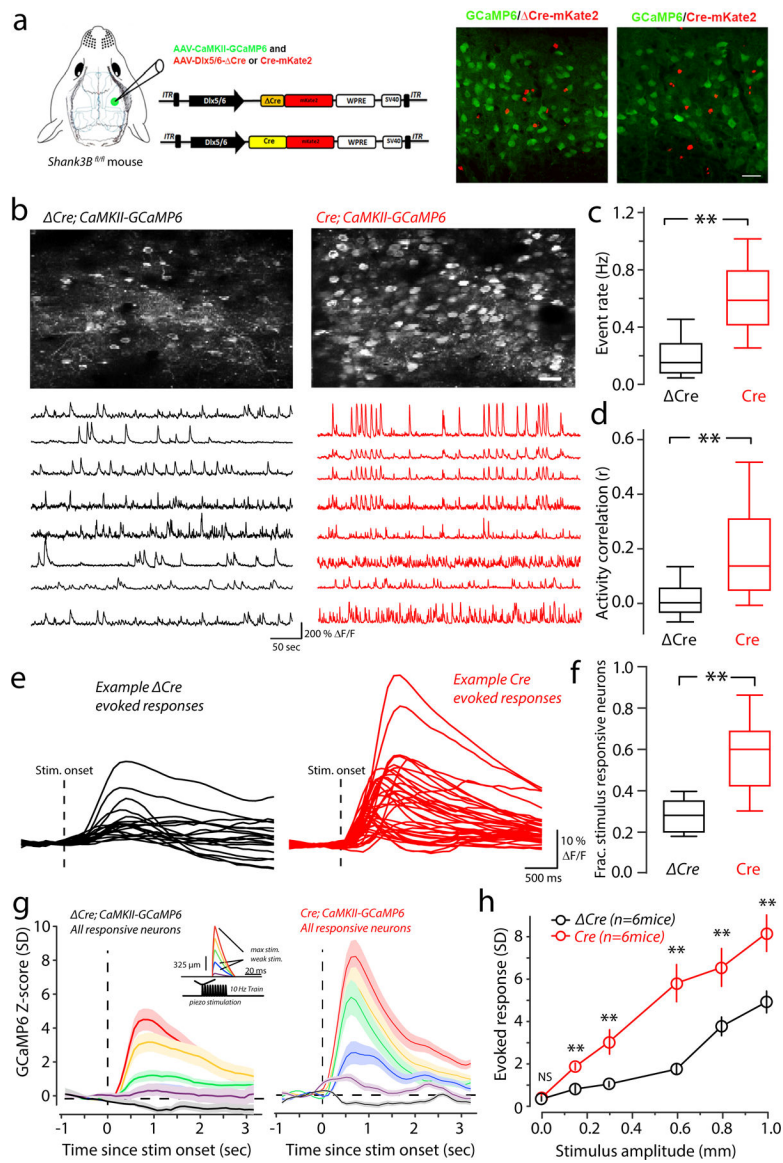
Figure 5. Preferential deletion of *Shank3* in vS1 interneurons also results in enhanced spontaneous and stimulus-evoked activity in excitatory neurons.

(**a**) Left panel: selective deletion of *Shank3* in the interneurons of somatosensory cortex was achieved by injection interneuron-specific AAV-Cre virus (AAV-Dlx5/6-Cre-mKate2 or AAV-Dlx5/6- Cre-mKate2 as control) in *Shank3B*^{fl/fl} mice. AAV-CaMKII-GCaMP6 (CaMKII-GCaMP6) virus was co-injected to monitor the neuronal activity in pyramidal neurons. Right panel: The confocal image of the GCaMP6(green) and Dlx5/6- Cre/Cre expression (red) in an AAV-Dlx5/6- Cre-mKate2 -injected (left) and AAV-Dlx5/6-Cre-mKate2-injected *Shank3B*^{fl/fl} mouse(right). (**b**) Upper: example mean two-photon CaMKII-GCaMP6 imaging fields from a Dlx5/6- Cre (left) and Dlx5/6-Cre-injected (right) mouse. Scale bar is 50 μm. Lower panels: example spontaneous F/F time-series traces from the upper imaging fields from Dlx5/6- Cre-injected (left) and Dlx5/6-Cre-injected (right) mouse. (**c**) Box-plots quantifying differences of spontaneous calcium event rate that was determined by counting the total number of deconvolved individual Ca^{2+}-events for ten

minutes (n=486 neurons from 6 Dlx5/6- Cre-injected mice; 510 neurons from 6 Dlx5/6-Cre-injected mice). Asterisk denotes a statistically significant difference between the sample groups (**p<0.0001; bootstrap mean-difference test). (**d**) The correlation between spontaneous firing was quantified as the Spearman's rank correlation coefficient (ρ) for all possible pairings in each imaging session, and then pooled across sessions. Box-plots show the distribution of all pooled correlations between Dlx5/6- Cre-injected (control group) and Dlx5/6-Cre-injected (local knockout group) excitatory neurons (n=38,874 pairs from 6 Dlx5/6- Cre-injected mice; 40,178 pairs from 6 Dlx5/6-Cre-injected mice), and show an overall increase in correlations among excitatory neurons in Dlx5/6-Cre-injected compared to Dlx5/6- Cre-injected. Asterisk denotes a statistically significant difference between the sample groups (**p<0.0001; bootstrap mean-difference test). (**e**) Example traces showing the F/F responses to maximal (1mm) whisker deflections stimulus of the responsive neurons from a representative Dlx5/6- Cre-injected (black) and Dlx5/6-Cre-injected(red) mice. The dashed line indicates the onset of the whisker stimulus. (**f**) Box-plots showing the fraction of neurons determined to be stimulus responsive in Dlx5/6- Cre-injected (black; n=6) and Dlx5/6-Cre-injected (red; n=6) mice. Asterisk denotes a statistically significant difference between the sample groups (Dlx5/6- Cre proportion = 0.16 ± 0.06, n= 6 mice; Dlx5/6-Cre proportion = 0.35±0.08, n=6 mice; **p<0.0001; bootstrap mean-difference test). (**g**) Left panel: The magnitude of evoked responses in Dlx5/6- Cre-injected mice, across the range of stimulus amplitudes. We quantified this by constructing peri-stimulus time histograms (PSTHs) from Z-scored evoked-responses for all of the responsive neurons (n=123 neurons from 6 Dlx5/6- Cre-injected mice and 188 neurons from 6 Dlx5/6-Cre-injected mice). The average response for each stimulus amplitude is color coded as indicated by the inset showing the piezo-stimulus waveform (red is the maximal deflection, purple is the weakest). Solid lines correspond to the mean and the colored shaded regions correspond to the standard error of the mean. Right panel: same as in *left panel*, but from Dlx5/6-Cre-injected. (**h**) Comparison of peak-evoked responses across the stimulus-amplitudes tested for all responsive neurons in Dlx5/6- Cre-injected (black; n=123 neurons from 6 mice) and Dlx5/6-Cre-injected (red; n=188 neurons from 6 mice) *Shank3B*^fl/fl^ mice. The center of the circles represents to the mean and the error bars represent to the standard error of the mean. Asterisks denote statistically significant differences (**p<0.0001, NS denotes no difference *p*>0.05; bootstrap mean-difference test, *p*-values in order from left-to-right: 0.5, <0.0001, <0.0001, <0.0001, <0.0001, <0.0001). These results repeated two times. Box-and-whisker plots show median values (middle vertical bar) and 25th (bottom side of the box) and 75th percentiles (top side of the box) with whiskers indicating the range. All bootstrap mean-difference tests were two-sided. Cre: AAV-Dlx5/6- Cre-mKate2-injected mouse group; Cre: AAV-Dlx5/6-Cre-mKate2-injected mouse group.
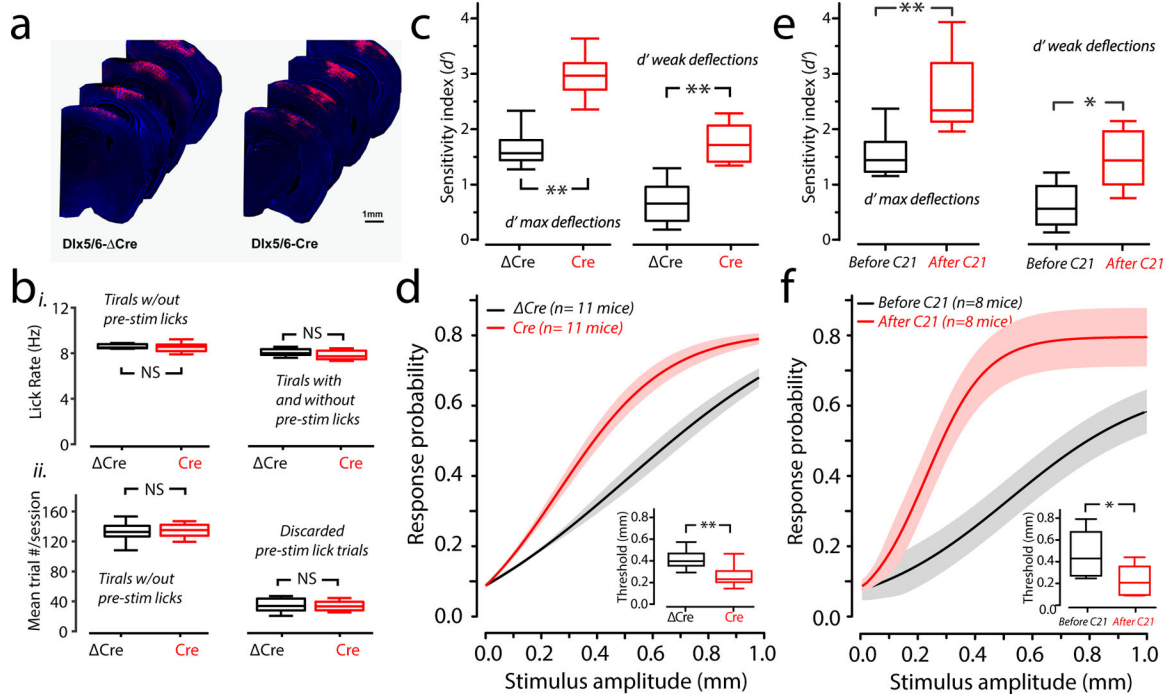
Figure 6. Preferential deletion of *Shank3* in Interneurons of vS1 leads to behavioral hyper-reactivity of the somatosensory system.

(**a**) *Shank3B*^{fl/fl} mice were injected with an AAV containing either a Dlx5/6-ΔCre or Dlx5/6-Cre construct in vS1. The image montage shows the extent of localization of ΔCre or Cre expression in two example mice. (**b**) *i*, Box-plots of mean lick rates for Dlx5/6-ΔCre (black) and Cre (red) injected animals. Left, average lick rate for trials that showed no pre-stimulus licking at all. Right, average lick rate including trials on the left and trials that showed pre-stimulus licking. In either case, there was no significant difference in lick rates (p=0.8 left, p=0.5 right; bootstrap mean-difference test). *ii*, left, Box-plots showing the number of trials per session completed by Dlx5/6-ΔCre (black; n=6 mice) and Dlx5/6-Cre (red; n =6 mice) injected animals. (p=0.7; bootstrap mean-difference test). Right, same as left, but the average number of trials with pre-stimulus licks (which were not analyzed). There was no significant difference (p=0.8; bootstrap mean-difference test). (**c**) *Left*, Box and whisker plots showing the bootstrap estimate of population mean d' for maximal stimuli for Dlx5/6-ΔCre (black; n=11 mice) and Dlx5/6-Cre (red; n=11 mice) injected animals. Right, same but showing *d'* for weak stimuli. There was a significant difference in both maximal *d'* (Dlx5/6-ΔCre mean ± s.e.m.: 1.59 ± 0.12; Dlx5/6-Cre: 2.92 ± 0.14, **p<0.0001, bootstrap mean-difference test) and weak *d'* (Dlx5/6-ΔCre mean ± s.e.m.: 0.65 ± 0.13; Dlx5/6-Cre: 1.73 ± 0.12; n=11 mice for each group; **p<0.0001, bootstrap mean-difference test). (**d**) Mean psychometric curves (non-normalized sigmoidal function fits) from the same sessions used in **c**. Solid lines denote the mean, and the shaded regions are the standard error of the mean. The inset show a significant difference of detection threshold between groups (**p<0.0001; bootstrap mean-difference test, Dlx5/6-ΔCre mean ± s.e.m.: 416 ± 31 μm; Dlx5/6-Cre: 266 ± 35 μm; n= 11 mice from each group). There was also a difference in the slope factors (Dlx5/6-ΔCre mean ± s.e.m.: 207 ± 13; Dlx5/6-Cre: 127 ± 17; n=11 mice in each group **p<0.0001, bootstrap mean-difference test). (**e**) Box and whisker plots showing the bootstrap estimate of

population mean d' maximal stimuli for the hM4Di-injected mice before (black) and after (red) C21 infusion (**p<0.0001, bootstrap mean-difference test; before-C21 mean ± s.e.m.: 1.58 ± 0.17; after-C21: 2.73 ± 0.31). *Right*, same but showing d' for weak stimuli (before-C21 mean ± s.e.m.: 0.62 ± 0.16; after-C21: 1.46 ± 0.21; n=8 mice; *p=0.0002, bootstrap mean-difference test). (**f**) Mean psychometric curves (non-normalized sigmoidal function fits) from the same sessions used in e. Solid lines denote the mean, and the shaded regions are the standard error of the mean. The inset show a significant difference of detection threshold between groups (pre-C21 mean ± s.e.m.: 525 ± 151 μm; post-C21: 233 ± 55 μm; n= 8 mice from each group; *p=0.004; bootstrap mean-difference test). The slope-factor was also significantly different (pre-C21 mean ± s.e.m.: 270 ± 65, post-C21: 114 ± 23; n=8 mice; p=0.02; bootstrap mean-difference test). These results repeated two times. Box-and-whisker plots show median values (middle vertical bar) and 25th (bottom side of the box) and 75th percentiles (top side of the box) with whiskers indicating the range. All bootstrap mean-difference tests were two-sided. Cre: AAV-Dlx5/6- Cre-mKate2-injected mouse group; Cre: AAV-Dlx5/6-Cre-mKate2-injected mouse group.